

1 **A Novel Hybrid Finite Element-Spectral Boundary Integral**  
2 **Scheme for Modeling Earthquake Cycles: Application to**  
3 **Rate and State Faults with Low-Velocity Zones**

4 **Mohamed Abdelmeguid<sup>1</sup>, Xiao Ma<sup>1</sup>, Ahmed Elbanna<sup>1</sup>**

5 <sup>1</sup>Department of Civil and Environmental Engineering, University of Illinois at Urbana-Champaign, Illinois, USA

6 **Key Points:**

- 7 • An efficient numerical scheme for modeling quasi-dynamic earthquake cycles.  
8 • Low-velocity fault zone change the behavior of earthquake sequence and aseismic slip.  
9 • Sub-surface events emerge for sufficiently compliant fault zone and lead to slip deficit.  
10 • Alternating event pattern is non-monotonically related to the compliant zone width.

11 This paper is a non-peer reviewed preprint submitted to EarthArXiv.

## Abstract

We present a novel hybrid finite element (FE) - spectral boundary integral (SBI) scheme that enables efficient simulation of earthquake cycles. This combined FE-SBI approach captures the benefits of finite elements in modelling problems with nonlinearities, as well as the computational superiority of SBI. The domain truncation enabled by this scheme allows us to utilize high-resolution finite elements discretization to capture inhomogeneities or complexities that may exist in a narrow region surrounding the fault. Combined with an adaptive time stepping algorithm, this framework opens new opportunities for modeling earthquake cycles with high-resolution fault zone physics. In this initial study, we consider a two dimensional (2-D) anti-plane model with a vertical strike-slip fault governed by rate and state friction in the quasi-dynamic limit under the radiation damping approximation. The proposed approach is first verified using the benchmark problem BP-1 from the Southern California Earthquake Center (SCEC) sequence of earthquake and aseismic slip (SEAS) community verification effort. The computational framework is then utilized to model the earthquake sequence and aseismic slip of a fault embedded within a low-velocity fault zone (LVFZ) with different widths and compliance levels. Our results indicate that sufficiently compliant LVFZs contribute to the emergence of subsurface events that fail to penetrate to the free surface and may experience earthquake clusters with nonuniform inter-seismic time. Furthermore, the LVFZ leads to slip rate amplification relative to the homogeneous elastic case. We discuss the implications of our results for understanding earthquake complexity as an interplay of fault friction and bulk heterogeneities.

## 1 Introduction

Earthquakes are among the costliest natural hazards on earth (D’Amico, 2016). The instabilities responsible for the onset and ensuing propagation of these events are linked to the fundamental physics of the heterogeneous and nonlinear topologically complex fault zones subjected to extreme geophysical conditions. Over sequences of seismic and aseismic slip, fault zones evolve continuously due to the feedback between nonlinear rheology, complex fault surface geometry, and both long range static and dynamic stress transfer. As there is insufficient data in the seismic catalog in the limit of large events (Lay, 2012), there is a strong need for developing computational tools that can accurately model the spatio-temporal patterns of earthquake ruptures and aseismic creep over long time scales and geologically relevant spatial scales to enable better understanding of these rare and large events, as well as to aid in policy making for hazard mitigation. However, this is far from being a trivial task due to the nonlinear and multi-scale nature of the problem.

The nonlinearity arises from a multitude of sources. Natural faults are usually embedded in a heterogeneous bed of rocks with variable elastic properties (Lewis & Ben-Zion, 2010; Yang et al., 2011) and a potential for yielding and fracture at different thresholds (Lyakhovskiy et al., 2016). Furthermore, in most cases, the fault friction depends on the slip, slip rate, and deformations time history (Dieterich, 1979; Di Toro et al., 2011; Goldsby & Tullis, 2011; Ben-David et al., 2010). The complex nature of this boundary condition makes an analytical solution only possible for a very limited number of model problems and necessitates solving the fracture problem numerically to predict the nucleation, propagation, and arrest conditions of the frictional instability (Nishioka & Atluri, 1982). The transitions in nonlinear rheology on fault surfaces, between rate weakening and rate strengthening, have been shown to contribute to the coseismic and inter-seismic slip evolution on the fault surface (Rice, 1993; Noda & Lapusta, 2013). However, off-fault properties and bulk heterogeneities may also play a significant role in altering the earthquake cycle pattern (Erickson & Day, 2016; Dolan & Haravitch, 2014; Cappa et al., 2014; Lindsey et al., 2014). For example, ruptures that would load the bulk beyond its elastic limit, leading to the development of in-elasticity or damage around the fault, may lock in nonuniform stresses on the fault surface that would impact subsequent ruptures (Erickson et al., 2017).

Another significant challenge in the modeling of sequences of seismic and aseismic slip in fault zones is bridging the scales, both spatially and temporally. Spatially, an earthquake may involve several kilometers of fault rupture, whereas the principal slip surfaces, where most of

66 the displacement is accommodated, may be in the order of a few millimeters (Rice, 2006).  
 67 Between the two length scales, several topological features, including branches, distributed dam-  
 68 age, and heterogeneous host rock, may exist (Chester et al., 1993; Rousseau & Rosakis, 2009;  
 69 Cochard & Rice, 2000; Barbot et al., 2009). Temporally, to simulate a spontaneous earthquake  
 70 sequence, the modeling approach should accommodate for slow tectonic loading during inter-  
 71 seismic creep that could take years, rupture nucleation spanning over a few days, as well as the  
 72 sudden release of energy associated with an earthquake rupture within seconds.

73 Earthquake cycle simulations, also referred to as sequences of earthquakes and aseismic  
 74 slip (SEAS) models, aim to study the long-term behavior of faults and lithospheric deforma-  
 75 tions on seismologically relevant spatio-temporal scales. They provide insight on the sponta-  
 76 neous nucleation and propagation of the seismic event, post-seismic response, and the aftershock  
 77 sequences. For most naturally-occurring earthquakes, identifying initial conditions is almost im-  
 78 possible, thus a need arises for simulations that would provide unbiased insight regardless of  
 79 the prescribed initial conditions. This is to be contrasted with simulations of a single seismic  
 80 event in which the results depend critically on the prescribed initial stress and fault state. While  
 81 in any SEAS simulation a portion of the earthquake sequence depends on the initial conditions  
 82 of the system at the start of the simulation, the overall pattern would converge to a statisti-  
 83 cally steady solution independent of the initial conditions after this transitional spin-up period.  
 84 Various numerical approaches have been developed toward simplifying the modeling process  
 85 of long term history of fault slip, mostly resorting to quasi-dynamic simulations that replace  
 86 inertial dynamics during rupture propagation with a radiation damping approximation (Tse  
 87 & Rice, 1986; Rice, 1993; Erickson & Dunham, 2014; Hillers et al., 2006; Y. Liu & Rice, 2007;  
 88 Luo & Ampuero, 2018). Other numerical approaches involve switching between quasi-static ap-  
 89 proximation during slow deformation to a fully dynamic representation once instability nucle-  
 90 ates (Okubo, 1989; Shibazaki & Matsu'ura, 1992; Kaneko et al., 2011; Duru et al., 2019). How-  
 91 ever, if this transition is done abruptly, it would introduce numerical artifacts that disrupt the  
 92 development of the instability. Lapusta et al. introduced a rigorous procedure for simulating  
 93 long term evolution of slip on planar faults in a homogeneous medium using a unified frame-  
 94 work for both inertial dynamics and quasi-static inter-seismic deformation (Lapusta et al., 2000).

95 Attempts to model earthquake cycles falls under two main categories: domain-based ap-  
 96 proaches and boundary integral approaches. Domain-based methods are flexible in handling  
 97 material nonlinearities and small-scale heterogeneities, as well as complexities of fault geom-  
 98 etry (Kuna, 2013; Taborda & Bielak, 2011). However, modeling earthquake cycles with such  
 99 methods is rare (Tong & Lavier, 2018; Biemiller & Lavier, 2017; Kaneko et al., 2008; Allison &  
 100 Dunham, 2018; Van Dinther et al., 2013), partially because discretization of the entire domain  
 101 is a computational bottleneck. To overcome one limitation of domain-based approaches that  
 102 stems from the need to fully discretize a very large domain, a wide breadth of research has been  
 103 directed toward finding appropriate truncation schemes that would shrink the simulated do-  
 104 main without affecting the physical solution, such as boundary viscous damping (Lysmer & Kuh-  
 105 lemeyer, 1969), infinite elements (Bettess, 1977), and perfectly matching layers (Berenger, 1994).  
 106 While these approaches provide an adequate fix to the main problem, the computational cost  
 107 would still be significant, as these absorbing boundaries need to be placed far away from the  
 108 fault surface to avoid compromising the accuracy of the solution. Furthermore, many of these  
 109 absorbing boundaries perform poorly in the quasi-static limit or if the incoming waves do not  
 110 have normal incidence on the boundary.

111 Alternatively, boundary integral techniques limit the computations to the fault plane, ef-  
 112 fectively reducing the dimensions of the problem; thus, reducing the computational cost (Aliabadi,  
 113 1997). Lapusta et al. managed to integrate a spectral formulation of the boundary integral equa-  
 114 tion (SBIE) method with a rigorous adaptive time-stepping scheme and introduced the concep-  
 115 t of mode-dependent truncation in the evaluation of the time integration of the convolution  
 116 integrals (Lapusta et al., 2000; Lapusta & Liu, 2009). Combining these features enabled long  
 117 duration computations with slow tectonic loading marked by spontaneous occurrences of dy-  
 118 namic rupture in problems with planar faults in homogeneous media. However, this approach  
 119 was only applicable to linear-elastic bulks. Furthermore, the lack of closed-form representation  
 120 for the Green's function in the majority of situations meant that the ability of the method to  
 121 provide well-defined solutions for domains with heterogeneities or fault roughness is compro-

122 mised. The difficulty associated with finding a convenient spectral transformation of the space  
 123 convolutions made computational investigation of problems with rough faults and fault zone  
 124 complexity extremely convoluted and at times impossible using the SBIE approach.

125 Hajarolasvadi and Elbanna (Hajarolasvadi & Elbanna, 2017) introduced a framework that  
 126 would consistently couple a domain-based approach (finite difference) and boundary integral  
 127 scheme (spectral boundary integral) in what the authors referred to as a hybrid scheme. The  
 128 proposed approach benefited from the strengths of each individual scheme without the draw-  
 129 backs associated with it. In this framework, the region of complexity or nonlinearity is confined  
 130 to a virtual strip that is discretized using finite difference. Through the consistent exchange of  
 131 boundary conditions, the virtual strip was then coupled to two linearly elastic half-spaces, whereas  
 132 the response of these half-spaces is captured by SBIE. This framework proved to yield accu-  
 133 rate results, at a fraction of the computational cost of a purely domain-based scheme. While  
 134 initially developed to study the elastodynamics of an anti-plane problem, Ma et al. extended  
 135 the hybrid method formulation to a 2-D in-plane setting and replaced the finite difference in  
 136 the bulk with a finite element formulation (Ma et al., 2018), enabling more flexibility in han-  
 137 dling complex boundaries and fault zone topologies (Ma & Elbanna, 2019).

138 In this paper, we extend the hybrid framework to model a sequence of earthquakes and  
 139 aseismic slip within the quasi-dynamic approximation. We focus our efforts in this initial study  
 140 on examining the influence of elastic heterogeneity on the quasi-dynamic earthquake sequence  
 141 that may emerge on a fault embedded in a low-velocity fault zone (LVFZ) undergoing slow tec-  
 142 tonic loading. The LVFZ are damaged regions surrounding primary slip surfaces in which the  
 143 seismic wave speed is lower than the that of the host rock, reflecting a more compliant struc-  
 144 ture. Low-velocity zones have been observed extensively, examples include San Andreas (Lewis  
 145 & Ben-Zion, 2010; Y.-G. Li & Leary, 1990), Calico (Cochran et al., 2009), and North Anato-  
 146 lian (Ben-Zion et al., 2003) fault zones and thus understanding their implication for earthquake  
 147 sequences is of special interest.

148 The remainder of the paper is organized as follows. In Section 2, we introduce the hybrid  
 149 numerical scheme. We then verify the numerical implementation for the method using a bench-  
 150 mark problem from SCEC SEAS community verification effort in Section 3.1. In Section 3.2,  
 151 we summarize our results for the contribution of different realizations of low-velocity fault zones  
 152 toward altering the sequence of earthquakes. We discuss the implications of our results and fu-  
 153 ture extensions of this initial study in Section 4. Section 5 is reserved for concluding remarks.  
 154

## 155 2 Problem Formulation and Computational Framework

### 156 2.1 Governing Equations

157 We consider a domain  $\Omega$ , with a prescribed traction boundary  $S_T$ , a displacement bound-  
 158 ary  $S_u$  and one or more internal surfaces of discontinuities, or faults, along the boundary  $S_f$ .  
 159 The equations of motion along with the appropriate boundary conditions are given by:

$$\begin{aligned}
 \rho \frac{\partial^2 u_i}{\partial t^2} - \frac{\partial \sigma_{ij}}{\partial x_j} - b_i &= 0 & \text{in } \Omega \\
 \sigma_{ij} n_j &= T_i & \text{on } S_T \\
 u_i &= u_i^0 & \text{on } S_u \\
 R_{ki}(u_i^+ - u_i^-) &= \delta_k, \quad T_i^{f+} = -T_i^{f-} & \text{on } S_f
 \end{aligned} \tag{1}$$

164 where  $u_i$  is the displacement vector, and  $b_i$  is the body force vector. Slip is defined by  $\delta_i = R_{ij}(u_j^+ -$   
 165  $u_j^-)$ , where  $R_{ij}$  is the rotation matrix that transforms the global coordinates to the local co-  
 166 ordinate system of the fault and superscripts + and - indicate the plus and minus sides of the  
 167 fault, respectively. If the fault plane is parallel to the  $x_1$  axis, the slip simplifies to  $\delta = u_1^+ -$   
 168  $u_1^-$ .  $\sigma_{ij}$  is the stress tensor. We assume body forces to be zero and the material behavior to be  
 169 linear elastic:

$$\sigma_{ij} = \lambda \delta_{ij} \varepsilon_{kk} + 2\mu \varepsilon_{ij} \tag{2}$$

171 where  $\varepsilon_{ij}$  is the infinitesimal strain tensor, and  $\mu$ , and  $\lambda$  are the Lamé parameters.

172 In this initial study, we restrict our implementation to the 2-D anti-plane shear deformation  
 173 problem, in which the only nonzero component of the displacement is restricted to the  $x_3$   
 174 direction. The body forces are assumed to be zero; accordingly, the balance of linear momen-  
 175 tum reduces to:

$$176 \quad \rho \frac{\partial^2 u_3}{\partial t^2} = \sigma_{13,1} + \sigma_{23,2} \quad (3)$$

177 where  $\tau_{13}$  and  $\tau_{23}$  are the shear components of stress. Considering only linearly elastic mate-  
 178 rials, the stress is given by:

$$179 \quad \sigma_{13} = \mu \frac{\partial u_3}{\partial x_1} \quad (4)$$

$$180 \quad \sigma_{23} = \mu \frac{\partial u_3}{\partial x_2} \quad (5)$$

182 where  $\mu$  is the shear modulus which can have spatial dependencies. By substituting in the bal-  
 183 ance equation we obtain:

$$184 \quad \rho \frac{\partial^2 u_3}{\partial t^2} = \frac{\partial}{\partial x_1} \left( \mu \frac{\partial u_3}{\partial x_1} \right) + \frac{\partial}{\partial x_2} \left( \mu \frac{\partial u_3}{\partial x_2} \right) \quad (6)$$

185 The slip constraint imposed on the governing equation then reduces to:

$$186 \quad R_{k3}(u_3^+ - u_3^-) = \delta_k \quad \text{on} \quad S_f \quad (7)$$

187 Our main goal is to provide an efficient and accurate numerical scheme that is capable of solv-  
 188 ing this set of equations in an unbounded domain.

## 189 **2.2 Hybrid Method Formulation**

190 The hybrid formulation considered here is a combination of the finite element method (FEM)  
 191 and the spectral boundary integral (SBI) method previously introduced by (Ma et al., 2018).  
 192 The nonlinearities, such as fault surface roughness or material nonlinearity, as well as small-  
 193 scale heterogeneities, are confined apriori in a virtual strip of a certain width. This virtual strip  
 194 is then discretized and modeled using FEM. The rest of the domain, which is homogeneous and  
 195 linear-elastic, is modeled using the SBI equation as two half-spaces and coupled to the FEM  
 196 domain on each side ( $S^+$ ,  $S^-$ ). The two methods enforce continuity by exchanging traction and  
 197 displacement boundary conditions at those sides. The general setup of the hybrid method is  
 198 shown in Figure 1. The width of the virtual strip depends on the nature of the problem and  
 199 may be adjusted to contain the heterogeneities, nonlinearities, and other fault zone complex-  
 200 ities.

### 201 **2.2.1 Finite Element Method**

202 The fault discontinuity implementation in the FEM is based on the domain decomposi-  
 203 tion approach outlined in (Aagaard et al., 2013). In this approach, the fault surface is consid-  
 204 ered to be an interior boundary between two domains with + and - sides. The slip on the fault  
 205 produces equal and opposite tractions on each of those sides, represented by a Lagrange mul-  
 206 tiplier. It follows that the weak form representation of this problem is give by:

$$207 \quad - \int_V \sigma_{ij} \phi_{i,j} dV + \int_{S_T} T_i \phi_i dS - \int_V \rho \ddot{u}_i \phi_i dV - \int_{S_{f+}} T_i^{f+} \phi_i dS + \int_{S_{f-}} T_i^{f-} \phi_i dS = 0 \quad (8)$$

208 where  $\phi$  is the weighting function. The integral along  $S_f$  accounts for the Lagrange multi-  
 209 pliers (tractions) on the fault surfaces.  $T_i^{f+} = \sigma_{ij} n_j^+$  and  $T_i^{f-} = \sigma_{ij} n_j^-$  where  $n_j^+$  and  $n_j^-$  are  
 210 the fault normals for the positive and negative sides of the faults respectively. These bound-  
 211 ary tractions are associated with the slip constraint on the fault shown in expression (7) and  
 212 are imposed via Lagrange multipliers.

213 To account for the coupling between the FEM and SBI equation within the finite element  
 214 formulation, we proceed as follows. We impose the tractions  $\tau^{SBI}$  that accounts for the exis-  
 215 tence of the half-spaces as Neumann boundary conditions for the FEM strip. The value of  $\tau^{SBI}$

216 is provided through the SBI formulation as will be discussed shortly. This ensures continuity  
 217 of traction at the outer interfaces. Since the nodes along the outer interfaces share the same  
 218 kinematic degrees of freedom between the virtual strip and the adjacent half-space, continu-  
 219 ity of displacements is also automatically satisfied. Altogether, this leads to the following sys-  
 220 tem of equations:

$$221 \quad - \int_V \sigma_{ij} \phi_{i,j} dV + \int_{S_{SBI}^+} \tau_i^{+,SBI} \phi_i dS - \int_{S_{SBI}^-} \tau_i^{-,SBI} \phi_i dS - \int_V \rho \ddot{u}_i \phi_i dV$$

$$222 \quad - \int_{S_{f+}} T_i^{f+} \phi_i dS + \int_{S_{f-}} T_i^{f-} \phi_i dS = 0 \quad (9)$$

$$223 \quad \int_{S_f} \phi_k [R_{ki}(u_i^+ - u_i^-) - d_k] = 0 \quad (10)$$

225 Here, we adopt a quasi-dynamic modeling framework where inertial effects are approx-  
 226 imated with a radiation damping term when resolving shear tractions on the fault surface. Thus,  
 227 time dependence enters through the constitutive models and the loading conditions only. While  
 228 not capturing the full dynamic nature of the problem, this assumption is important since sup-  
 229 pressing inertial terms entirely would result in an unbounded slip rate in finite time (Rice, 1993).  
 230 The quasi-dynamic simulations reduce then to a series of static problems with potentially time-  
 231 varying physical properties and boundary conditions. The temporal accuracy of the solution  
 232 is limited to resolving these temporal variations. Considering deformations at time  $t$  and af-  
 233 ter suppressing the inertia term, the weak form may be written as:

$$234 \quad - \int_V \sigma_{ij}(t) \phi_{i,j} dV + \int_{S_{SBI}^+} \tau_i^{+,SBI}(t) \phi_i dS - \int_{S_{SBI}^-} \tau_i^{-,SBI}(t) \phi_i dS$$

$$235 \quad - \int_{S_{f+}} T_i^{f+}(t) \phi_i dS + \int_{S_{f-}} T_i^{f-}(t) \phi_i dS = 0 \quad (11)$$

$$236 \quad \int_{S_f} \phi_k [R_{ki}(u_i^+(t) - u_i^-(t)) - d_k(t)] = 0 \quad (12)$$

238 with the understanding that fault tractions will be modified to account for radiation damping  
 239 effects as we will describe shortly. Expressions (11) and (12) may be discretized using a Galerkin  
 240 approach. Accordingly, we express the test function  $\phi$ , trial solution  $u$ , Lagrange multipliers  
 241  $T^f$ , fault slip  $d$ , and SBI tractions  $\tau^{SBI}$  as linear combinations of basis function  $N(x)$ :

$$242 \quad \phi = \sum_m w_m N_m(x_i), \quad u = \sum_n u_n N_n(x_i), \quad T^f = \sum_p T_p^f N_p(x_i),$$

$$243 \quad \tau^{SBI} = \sum_s \tau_s^{SBI} N_s(x_i), \quad d = \sum_p d_p N_p(x_i) \quad (13)$$

244 The subscripts denote the number of basis functions, where  $n$  is the number of functions as-  
 245 sociated with the domain displacements,  $p$  is the number of functions associated with fault sur-  
 246 face,  $m$  is the number of basis functions for the test solutions, and  $s$  denotes the functions as-  
 247 sociated with the SBI degree of freedoms. In the presented numerical models, linear Lagrange  
 248 basis functions are utilized for the spatial discretization of the simulated domain. Noting that  
 249 the tractions on the fault are equal in magnitude, the weak form is transformed into:

$$250 \quad - \int_V \nabla N_m^T \cdot \sigma(t) dV + \int_{S_{SBI}^+} N_m^T N_{s+} \tau_s^{SBI}(t) dS - \int_{S_{SBI}^-} N_m^T N_{s-} \tau_s^{SBI}(t) dS$$

$$251 \quad - \int_{S_{f+}} N_m^T N_p T_p^f(t) dS + \int_{S_{f-}} N_m^T N_p T_p^f dS = 0 \quad (14)$$

$$252 \quad \int_{S_f} N_p^T [R_{pn}(N_n u_n^+(t) - N_n u_n^-(t)) - N_p d_p(t)] = 0 \quad (15)$$

254 Assuming that the fault surface is aligned with the domain coordinate system these expressions  
 255 are converted to a more compact matrix notation as:

$$256 \quad \mathbf{K}u(t) + \mathbf{L}^T (\tau^{SBI}(t) + T^f(t)) = \mathbf{F}(t) \quad (16)$$

$$257 \quad \mathbf{L}u(t) = \mathbf{D}(t) \quad (17)$$

259 In this problem, the unknowns are the bulk displacement  $u_n$ , the fault tractions (Lagrange mul-  
 260 tipliers)  $T^f$ , and SBI tractions  $\tau^{SBI}$ . On the fault surface  $S_f$ , we prescribe slip  $d$  based on ex-  
 261 plicit time integration of the slip rate. The fault tractions are then solved for as part of the un-  
 262 knowns in the linear system of equations (16). The fault constitutive law then dictates the de-  
 263 pendency of the fault tractions on the slip rate and state variable, which we utilize to solve for  
 264 the slip rate and march forward in time once we obtain the solution for the fault tractions. The  
 265 full details of our algorithm are outlined in Section 2.2.4.

### 266 *2.2.2 Spectral Boundary Integral Method*

267 The boundary integral method has been used extensively since the mid-1980s to study  
 268 the propagation of cracks (Aliabadi, 1997; Barbot, 2018). The main advantage of this method  
 269 is that it eliminates the need to study wave propagation in the entire domain by using integral  
 270 relationships between the displacement discontinuities and tractions along the crack path (Day  
 271 et al., 2005). The spectral formulation of this method gives an exact form of such a relation-  
 272 ship in the Fourier domain. We use the spectral formulation introduced in (P. Geubelle & Rice,  
 273 1995), where the elastodynamic analysis of each half-space is carried out separately. In view  
 274 of the hybrid method, where SBI equation constitutes a boundary condition to the FEM model  
 275 through tractions  $\tau^{SBI}$ , we focus the description on modeling a half-space. For brevity, we re-  
 276 strict our discussion to the anti-plane formulation of the SBI scheme. However, we note that  
 277 the formulation of the independent SBI equation for a three-dimensional (3-D) domain may be  
 278 readily incorporated in the hybrid scheme (Breitenfeld & Geubelle, 1998). The relationship be-  
 279 tween the traction  $\tau_3$  and the resulting displacements at the boundary of a half-space may be  
 280 expressed as:

$$281 \quad \tau_3^\pm(x_1, t) = \tau_3^{0\pm}(x_1, t) \mp \frac{\mu}{c_s} \dot{u}_3^\pm(x_1, t) \pm f_3^\pm(x_1, t) \quad (18)$$

282 where,  $\tau_3^0(x_1, t)$  is the shear stress that would be present if the fault is locked,  $c_s$  is the shear  
 283 wave speed, and  $f_3^\pm(x_1, t)$  is a functional given by the space time convolution of the fundamen-  
 284 tal elastodynamic solution with prior history of slip along the fault line. This convolution term  
 285 is expressed in the Fourier domain as:

$$286 \quad f_3^\pm(x_1, t) = F_3^\pm(t; q) e^{iqx_1} \quad (19)$$

287 where  $q$  is the wave number. The Fourier coefficient  $F_3^\pm(t; q)$  is given in terms of displacement  
 288 Fourier coefficient  $U_3(t; q)$  by the convolution integral (P. H. Geubelle & Breitenfeld, 1997):

$$289 \quad F_3^\pm(t; q) = \mp \mu |q| \int_0^t H_{33}(|q|c_s t') U_3^\pm(t - t'; q) |q| c_s dt' \quad (20)$$

290 The convolution kernel of this independent formulation was shown to be  $H_{33}(T) = J_1(T)/T$   
 291 with  $J_1(T)$  as the first kind Bessel function of order one. This is identical to the convolution  
 292 kernel of the combined formulation for the anti-plane problem (Lapusta et al., 2000).

293 Integration by parts would yield an analogous "velocity" representation in terms of  $\dot{U}_3(t; q)$   
 294 that distinguishes between the static and dynamic contributions.

$$295 \quad F_3^\pm(t; q) = \mp \mu |q| U_3(t; q) \pm \mu |q| \int_0^t W_{33}(|q|c_s t') \dot{U}_3^\pm(t - t'; q) |q| c_s dt' \quad (21)$$

296 where  $W_{33}(p) = \int_p^\infty H_{33}(T) dT$ . The SBI equation may then be readily adjusted for the quasi-  
 297 dynamic framework by only considering the static contribution of the convolution term  $f_3(x_1, t)$ .

298 In this case, the Fourier coefficient  $F_3(t; q)$  is given by:

$$299 \quad F_3^\pm(t; q) = \mp \mu |q| U_3(t; q) \quad (22)$$

300 The interested reader is referred to equation 6 in (Cochard & Madariaga, 1994) for the expres-  
301 sion of the convolution kernels in the space time domain for the 2-D anti-plane problem.

### 302 **2.2.3 Frictional Framework**

303 Here, we adopt a rate and state frictional (RSF) formulation (Dieterich, 1979; Ruina, 1983).  
304 The boundary condition on the fault surface is enforced by equating the fault shear stress to  
305 its strength:

$$306 \quad \tau = F(V, \theta) = f(V, \theta) \sigma_n \quad (23)$$

307 where the fault strength  $F$  is defined in terms of the normal stress  $\sigma_n$  and the friction coeffi-  
308 cient  $f$ . In the RSF, the friction coefficient depends on the slip rate  $V$  and state  $\theta$  as:

$$309 \quad f(V, \theta) = f_o + a \ln \left( \frac{V}{V_o} \right) + b \ln \left( \frac{\theta V_o}{L} \right) \quad (24)$$

310 where  $L$  is the characteristic slip distance,  $f_o$  is the reference friction coefficient defined at a  
311 slip rate  $V_o$ . The state evolution is prescribed through the aging law (Rice & Ruina, 1983), which  
312 is commonly applied to earthquake cycle simulations (Lapusta et al., 2000; Erickson & Dun-  
313 ham, 2014; Herrendörfer et al., 2018; Y. Liu & Rice, 2007) and defined as:

$$314 \quad \frac{d\theta}{dt} = 1 - \frac{V\theta}{L} \quad (25)$$

315 This results in a steady-state solution of the state variable  $\theta_{ss} = \frac{L}{V}$ . The corresponding steady-  
316 state friction coefficient is given by:

$$317 \quad f_{ss} = f_o + (a - b) \ln \left( \frac{V}{V_o} \right) \quad (26)$$

318 Here, the parameter combination  $a - b > 0$  describes a steady state rate-strengthening frictional  
319 response and  $a - b < 0$  describes a steady state rate-weakening frictional response.

320 In expression (24), the fault frictional strength becomes ill-posed at  $V = 0$ . There are  
321 various alternative rate and state formulations that allow for solutions near  $V = 0$  (Ampuero  
322 & Ben-zion, 2008; Barbot, 2019; Bizzarri, 2011). However, in this analysis, we follow the reg-  
323 ularized version of the RSF presented in (Rice & Ben-Zion, 1996):

$$324 \quad f(V, \theta) = a \sinh^{-1} \left[ \frac{V}{2V_o} \exp \left( \frac{f_o + b \ln \left( \frac{\theta V_o}{L} \right)}{a} \right) \right] \quad (27)$$

325 Using an energy balance approach, Ampuero et al. established the following theoretical  
326 estimate for the nucleation size  $h^*$  of an anti-plane frictional crack under slow tectonic load-  
327 ing (Ampuero & Rubin, 2008):

$$328 \quad h^* = \frac{2\mu L b}{\pi \sigma_n (b - a)^2} \quad (28)$$

329 This nucleation size defines the critical wavelength that has to be resolved within the numer-  
330 ical scheme and is valid for  $a/b > 0.5$ .

331 In addition to the nucleation size, Dieterich presented another characteristic length scale  
332  $L_b$ , which is associated with the process zone during the propagation of the rupture when  $V\theta/L \gg$   
333 1 and scales as  $b^{-1}$  (Dieterich, 1992). For anti-plane perturbations  $L_b$  is given as:

$$334 \quad L_b = \frac{\mu L}{\sigma_n b} \quad (29)$$

335 It is vital to properly resolve this length scale as it is more stringent than the nucleation zone's  
 336 length. In our computational framework we always ensure that  $h^*$  and  $L_b$  are both well resolved.  
 337

### 338 **2.2.4 Time Stepping**

339 To predict the response of the domain at  $t+\Delta t$ , we solve the system of equations in ex-  
 340 pressions (16) and (17) starting from a known state at time  $t$ , including slip  $d(t)$  and state vari-  
 341 able  $\theta(t)$ , and subjected to a time-dependent boundary condition  $u_b(t)$  on  $S_u$  and traction bound-  
 342 ary conditions  $\tau^{SBI}(t)$  on the virtual boundaries. The updating algorithm is then given as fol-  
 343 lows:

- 344 1. Use  $u(t - \Delta t)$  as a predictor for  $u(t)$  on  $S_{SBI}$ .

$$345 \quad u_{SBI}^*(t) = u_{SBI}(t - \Delta t) \quad (30)$$

- 346 2. Make a corresponding prediction for the convolution functional  $f^*(t)$  using the displace-  
 347 ment assumption (30). This is done by computing the Fourier coefficients of  $u^*(t)$  such  
 348 that:

$$349 \quad u_{SBI}^*(t) = \sum_{s=-n_s/2}^{n_s/2} U_s^*(t) e^{iq_s z}, \quad q_s = \frac{2\pi s}{\lambda} \quad (31)$$

350 where  $\lambda$  is the length of the SBI domain under consideration, and  $n_s$  is the number of  
 351 FFT sample points used to discretize the domain. Then, using expression (22), we com-  
 352 pute the Fourier coefficients of the functional.

$$353 \quad F_s^*(t; q) = \mp \mu |q_s| U_s^*(t; q) \quad (32)$$

354 The functional is then recovered in the real space using inverse FFT as:

$$355 \quad f^*(t) = \sum_{s=-n_s/2}^{n_s/2} F_s^*(t) e^{iq_s z} \quad (33)$$

- 356 3. Write  $\tau^{SBI*}(t)$  assuming no initial tractions imposed on  $S_{SBI}$  as:

$$357 \quad \tau^{SBI*,\pm}(t) = \mp \frac{\mu}{c_s} \dot{u}_{SBI}(t) + f^*(t) \quad (34)$$

358 where  $\dot{u}_{SBI}(t)$  is still an unknown quantity that depends on  $u_{SBI}(t)$ . Thus, we use a back-  
 359 ward Euler approximation:

$$360 \quad \dot{u}_{SBI}(t) = \frac{u_{SBI}(t) - u_{SBI}(t - \Delta t)}{\Delta t} \quad (35)$$

- 361 4. Find a new prediction for  $u^{**}(t)$  by solving the elasticity equations in expressions (16)  
 362 and (17) now rearranged as:

$$363 \quad \mathbf{K}u^{**}(t) + \mathbf{L}^T \left( \mp \frac{\mu}{c_s \Delta t} u_{SBI}^{**}(t) + T^f(t) \right) = \mathbf{F}(t) - \mathbf{L}^T \left( \pm \frac{\mu}{c_s \Delta t} u_{SBI}(t - \Delta t) + f^*(t) \right) \quad (36)$$

$$364 \quad \mathbf{L}u(t) = \mathbf{D}(t) \quad (37)$$

- 365 5. Correct  $u_{SBI}(t)$  by using both predictions:

$$367 \quad u_{SBI}(t) = \frac{1}{2} [u_{SBI}^*(t) + u_{SBI}^{**}(t)] \quad (38)$$

- 368 6. Repeat Steps 2-4 using the corrected  $u_{SBI}(t)$  and obtain fault tractions  $T^f$  from the La-  
 369 grange multipliers.  
 370 7. Find the value of the slip rate  $V(t)$  corresponding to fault tractions  $T^f$ . This is done in  
 371 a quasi-dynamic framework by equating the fault tractions to the fault strength plus ra-

372 diation damping component to get:

$$373 \quad T^f = F(V, \theta) + \eta V \quad (39)$$

374 where  $\eta = \mu/2c_s$  is half the shear-wave impedance,  $\mu$  is the shear modulus, and  $c_s$  is  
 375 the shear wave speed of the elements adjacent to the fault. This is a nonlinear equation  
 376 that we solve using a safe-guarded Newton-Raphson scheme (quadratic convergence), with  
 377 the safe-guard being an embedded Secant scheme (superlinear convergence).

- 378 8. Steps 1-7 are evaluated at each increment within a Runge-Kutta-Fehlberg (RKF45) time  
 379 stepping algorithm to march the system forward to time  $t+\Delta t$ . The RKF45 is an adap-  
 380 tive time stepping procedure that is fourth order accurate with a fifth order accurate er-  
 381 ror estimate.
- 382 9. Return to step 1 to proceed further in time

383 To ensure accuracy, we restrict our time step to a fraction of  $L/V$  such that the slip increment  
 384 in a time step is bounded to be smaller than the characteristic length scale in the rate and state  
 385 friction law. Here, we choose this upper bound following (Lapusta et al., 2000) but other op-  
 386 tions will be further investigated in the future.

387 Algorithm 1 outlines the entire proposed procedure in which we time march from a given  
 388 start at time  $t$  to  $t + \Delta t$ .

---

**Algorithm 1: Time Advance Algorithm**

---

```

while  $t < t_{final}$  do
  At time  $t$ ,  $d(t)$ ,  $\theta(t)$ ,  $u_b(t)$  and  $u(t - \Delta t)$  are known;
  Initialize RKF45 algorithm with relative tolerance  $10^{-7}$ ;
  for  $t \rightarrow t + \Delta t$  do
    1. Using  $u^*(t)$  estimate  $\tau_s^{SBI^*}(t)$ ;
    2. Solve the linear equations (36) and (37) for  $u^{**}(t)$ ;
    3. Obtain a correction for  $\tau_s^{SBI^{**}}(t)$  based on  $u(t) = \frac{1}{2} [u^{**}(t) + u^*(t)]$ ;
    4. Re-solve the linear equations (36) and (37) for  $u(t)$  and  $T^f(t)$ ;
    5. Use  $T^f(t)$  to solve expression (39) for  $V(t)$ ;
    6. Repeat Steps 1-5 at every RKF45 increment of time;
    7. Estimate the subsequent  $\Delta t$  using the error measure;
  end
  Update state and proceed further in time;
end

```

---

390 While in Algorithm 1 a single corrections step is described, further corrections may be used  
 391 to improve the accuracy of the algorithm. However, further correction steps did not show any  
 392 substantial improvements on the result to merit the computational cost.

### 393 **3 Results**

394 To demonstrate the capabilities of the proposed scheme we consider two different prob-  
 395 lems. In the first one, we verify the numerical scheme using the SCEC SEAS Benchmark Prob-  
 396 lem BP-1 (Erickson & Jiang, 2018). In the second one, we investigate sequence of earthquakes  
 397 and aseismic slip on a fault embedded in a low-velocity zone (LVZ).

#### 398 **3.1 SCEC SEAS Benchmark Problem Verification**

399 We verify the hybrid scheme quasi-dynamic formulation using the benchmark problem BP-  
 400 1 from the SCEC SEAS Validation Exercise. This benchmark problem describes a 2-D anti-  
 401 plane shear problem, with a vertical strike-slip fault in a homogeneous half-space (see Figure  
 402 2a). The fault friction is governed by the regularized rate and state friction model with the ag-  
 403 ing law. The rupture is driven by slow tectonic loading defined by a constant plate velocity  $V_p$   
 404 imposed at a depth below the fault segment  $W_f$ , this allows for the aseismic creep to penetrate

405 into the fault and eventually cause rupture. The parameters of the simulation is summarized  
406 in Table 1.

407 In addition to a prescribed slip rate beneath the fault, a free surface lies at  $z = 0$ . The  
408 frictional parameters on the fault vary along the depth of the domain. The frictional proper-  
409 ties within region  $[0, H]$  are defined by  $a-b < 0$ , describing a velocity-weakening (VW) patch;  
410 with a velocity-strengthening (VS) patch for the region between  $[H+h, W_f]$ , and a linear tran-  
411 sition of length  $h$  between the two. The domain of the problem is defined by  $(x, y, z) \in (-\infty, \infty) \times$   
412  $(-\infty, \infty) \times (0, \infty)$ . The hybrid setup for this verification exercise is illustrated in Figure 2a.  
413 The virtual strip is discretized using FEM and the exchange of boundary conditions occur at  
414 surfaces  $S^+$  and  $S^-$ . The choice of the width of the FEM strip in this case is arbitrary since  
415 this is a homogeneous linear-elastic domain, and we will show that the results indeed do not  
416 depend on the location of this far-field boundary. The dimensions of the simulated problem will  
417 vary to include a finite depth  $L_z$ . The free surface is incorporated directly in the FEM formu-  
418 lation. To account for the free surface in the SBI formulation, we use the method of images and  
419 map the slip and the slip rate from the physical domain  $[0, L_z]$  to  $[-L_z, 0]$  when conducting the  
420 Fourier space calculation. Accordingly, the spatial domain in the SBI is considered as  $[-L_z, L_z]$ .  
421 This implies that the periodicity of the SBI domain is imposed on the total domain  $[-L_z, L_z]$ ;  
422 we rely on the large domain and uniform loading beyond the fault  $[W_f, L_z]$  to remedy the mis-  
423 match in boundary conditions between the two formulations. In our simulations, we always ensure  
424 that loading region  $W_l$  is sufficiently large, so that the solution is independent of our choice  
425 of  $L_z$ .

426 Figure 3 shows a comparison of the results from the hybrid scheme with those of a pure  
427 SBI formulation similar to the one in (Lapusta et al., 2000). Figure 3a, 3b, and 3c illustrate  
428 the time history plots of the slip rate and shear traction at stations  $z = 0, 7.5, 17.5$  km re-  
429 spectively. The results show excellent agreement between the SBI and hybrid solutions. Fig-  
430 ure 4a shows the time history for the surface slip rate at two different levels of the discretiza-  
431 tion for hybrid scheme and demonstrates its convergence to the high resolution pure SBI so-  
432 lution as the mesh is refined.

433 A significant advantage of the hybrid method is its capability to truncate the domain with-  
434 out incurring any accuracy drawbacks from the virtual boundary. To be able to model this prob-  
435 lem using a full finite element model would require a domain of  $80 \text{ km} \times 80 \text{ km}$  to ensure that  
436 the far field boundaries would not influence the fault behavior. However, in the hybrid scheme,  
437 the virtual boundary is chosen, arbitrarily, to be  $0.5 \text{ km}$  from the fault plane. Accordingly, within  
438 the FEM strip, we only need to discretize a domain of  $80 \text{ km} \times 1 \text{ km}$ . Although the problem  
439 under consideration is linear-elastic, it serves the purpose of validating the truncation efficiency  
440 of the hybrid scheme. When extrapolated to more complex scenarios, this efficient near-field  
441 truncation allows the finite element discretization to be limited within a small strip, leading  
442 to potential savings in both computational time and memory cost.

443 The coupling procedure between the FEM and SBI method is based on the communica-  
444 tion of boundary conditions across the virtual boundaries. Ideally, the solution should not de-  
445 pend on the location of either surfaces. To verify this point, we consider varying the width of  
446 the FEM strip denoted as  $W_s$ . Figure 4b shows the time history of surface slip rate for two sim-  
447 ulations, one with  $W_s = 1 \text{ km}$  and another with  $W_s = 10 \text{ km}$ . The results suggest there ex-  
448 ists no dependence for the solution on the virtual strip thickness.

### 449 3.2 Fault Embedded in a Low-Velocity Zone

450 Numerous field observations indicate the existence of complex crustal structures with het-  
451 erogeneous fault zones that evolve due to damage accumulation from repeated earthquakes. In  
452 particular, the so called low-velocity fault zones (LVFZs) exist in most mature faults. Within  
453 these zones, the wave velocity is estimated to be reduced by 20 to 60 % relative to the host rock  
454 (Huang et al., 2014, 2016; Barbot et al., 2008). The contrast may impact the long-term behav-  
455 ior of the earthquake cycles, resulting in complex patterns, as well as an increase in the slip due  
456 to the added compliance of these low-velocity regions.

457 To demonstrate the merit of the hybrid scheme developed in Section 2 and verified in Section 3.1, we consider a variation on the theme of the problem outlined in SCEC SEAS BP-1.  
 458 Here, the rate and state fault is embedded in a LVFZ with varying material properties. Fig-  
 459 ure 2b demonstrates the hybrid setup specialized for low-velocity fault zones. The low-velocity  
 460 zone may be viewed as a damaged region surrounding the fault with rigidity  $\mu_D$ , shear veloc-  
 461 ity  $c_s^D$ , and half width  $W$ ; sub- and superscript  $D$  will be used to describe properties within  
 462 the LVFZ.  
 463

464 Three different rigidity contrasts  $\mu_D/\mu$  are considered: 80%, 60%, and 40%. Under the  
 465 assumption of fixed density, the change in the shear modulus is accompanied by a change in  
 466 shear wave speed that would impact the shear wave impedance in the radiation damping com-  
 467 ponent of the fault strength. The host rock is assumed to have a fixed shear modulus of 33 GPa.  
 468 To account for the impact of the LVFZ width, several cases within each contrast is considered.  
 469 We note that the width of the virtual strip may be taken equal to the width of the LVFZ, that  
 470 is  $W = W_s/2$ . However, in our analysis, we introduced a buffer zone between the boundary  
 471 of the LVFZ and the virtual strip boundaries  $S^+$  and  $S^-$ . To make sure that the solution is  
 472 independent of the buffer zone dimension, we have checked the results for various buffer zone  
 473 thicknesses and obtained identical results. Except for the introduction of the LVFZ, all param-  
 474 eters used in the problem setup for this study is based on the SCEC SEAS benchmark exer-  
 475 cise summarized in Table 1.

476 To facilitate the comparison between different cases, we utilize the dimensionless param-  
 477 eters  $\mu_D/\mu$  and  $W/h^*$ . Here,  $h^*$  represents the estimated nucleation length of the layered me-  
 478 dia. The nucleation length estimate in expression (28) predicts the nucleation size based on a  
 479 fault embedded in a homogeneous medium. The introduction of LVFZ changes the nucleation  
 480 size such that we recover the nucleation size of an undamaged homogeneous media  $h_{hom}^*$  in the  
 481 limit  $W \rightarrow 0$  but recover the nucleation size of a damaged homogeneous media  $h_{hom}^{*D}$  in the  
 482 limit  $W \rightarrow \infty$ . To ensure accuracy and consistency it is thus crucial to identify the variation  
 483 in nucleation size and resolve the mesh accordingly. (Kaneko et al., 2011) provided the follow-  
 484 ing estimate for the nucleation size in this case based on linear stability analysis of a rate and  
 485 state fault embedded in a layered medium. The undamaged homogeneous media nucleation size  
 486 can be estimated using the fault properties presented in Table 1 to be  $h_{hom}^* = 1958$  m.

$$487 \quad h^* \tanh \left[ W \frac{\pi}{2h^*} + \tanh^{-1} \left( \frac{\mu_D}{\mu} \right) \right] = h_{hom}^{*D} \quad (40)$$

488 We solve the above equation numerically and use the resulting estimate to normalize the  
 489 width of the LVFZ.

### 490 **3.2.1 Mild Rigidity Contrast: $\mu_D/\mu = 0.8$**

491 In this section, we consider a LVFZ with mild contrast between the damaged media and  
 492 the host rock. We compare the earthquake sequence for two cases: a case with LVFZ of width  
 493 ratio  $W/h^* = 0.17$ , and a case with a homogeneous bulk and width ratio  $W/h^* = 0$ . Figure  
 494 5 shows the variation in surface slip rate profiles between the two cases. Since the rigidity varies  
 495 mildly, the two solutions are similar with minor variations in the peak slip rate and inter-event  
 496 time.

497 To get further insights into the impact of the LVFZ on the earthquake sequence, Figure  
 498 6a shows that with varying the width of the LVFZ,  $W$ , the characteristics of the earthquake  
 499 sequence changes, including the peak slip rate, and inter-event time.

500 For example, Figure 6b suggests that the peak slip rate increases as the LVFZ width in-  
 501 creases. The rate of change of the peak slip rate with width is high at small widths and becomes  
 502 negligible in the limit of large LVFZ widths. In the current framework, this behavior may be  
 503 explained by considering the following estimate for the slip rate based on fracture mechanics  
 504  $V \propto \Delta\tau c_R/\mu$ , where  $c_R$  is the rupture velocity. Thus, the velocity depend on the stress drop  
 505  $\Delta\tau$ , the rupture speed and the shear modulus. The current choice of the radiation damping  
 506 term ensures that the rupture speed is bounded by the shear wave speed which in turn is pro-

portional to the square root of the shear modulus (Rice, 1993). Thus,  $V \propto \Delta\tau/\sqrt{\mu}$ . As the width of the LVFZ increases, the effective shear modulus, on short wavelengths relevant to the crack tip propagation, decreases and eventually saturates at the value corresponding to the compliant region. The stress drop, however, remains almost invariant since it is constrained by the rate and state friction law which is weakly sensitive to variations in slip rate (the stress drop may slightly increase as the velocity increases, due to the logarithmic nature of the rate and state friction law). It follows that  $V \propto 1/\sqrt{\mu_{eff}}$  where,  $\mu_{eff}$  is the effective shear modulus over short wavelengths comparable to the process zone. As the width of the LVFZ increases from zero to the order of the process zone, the effective shear modulus rapidly decreases and the variation in the peak slip rate is more pronounced. As the width increases further to multiples of that length scale, the effective shear modulus approaches a constant value and the peak slip rate effectively saturates.

Furthermore, Figure 6c shows the non-monotonic dependence of the steady-state inter-event time  $T_c$  on the widths of the LVFZ  $W$ . Initially with the introduction of the LVFZ, a reduction in inter-event time is observed. The initial drop in the inter-event time may be associated with the reduction in the nucleation size due to the introduction of LVFZ. Thus the instability may be achieved faster as a smaller length scale needs to be destabilized. However, this pattern does not persist and is eventually reversed with larger-widths LVFZ showing longer inter-event times. This increase in the inter-event time may be explained by identifying that the loading of the fault is being applied through a constant plate loading rate imposed on a softer medium when the LVFZ is present. The stressing rate drops as the rigidity of the bulk drops. The effective rigidity of the medium, over long wavelengths relevant to the slow tectonic loading, decreases as the width of the LVFZ increases. The corresponding reduction in the stressing rate implies that it takes a longer time to accumulate the same amount of stress required for initiating the instability with the increased width of the LVFZ. In a simple quasi-dynamic model one would expect that inter-event time is inversely proportional to the stressing rate, that is  $T_c \propto 1/\dot{\tau}$ .

### 3.2.2 Intermediate Rigidity Contrast: $\mu_D/\mu = 0.6$

Here, we consider a LVFZ with a material contrast of  $\mu_D/\mu = 0.6$  and different values of  $W/h^*$ . Figure 7a demonstrates that by introducing a wide enough LVFZ, the resultant sequence of events may vary significantly. Specifically, the surface slip rate is compared for the following three cases: (1) homogeneous medium without damage, (2) a small LVFZ width with  $W/h^* = 0.04$  and (3) a slightly wider LVFZ with  $W/h^* = 0.08$ . Results for cases (1) and (2) are almost identical with just a minor variation in the inter-event time and the peak slip rate. However, as the width of the LVFZ  $W/h^*$  further increases, as in case (3), the results qualitatively change. In particular, we observe a kink in the surface slip rate profile that represents a slight increase in the slip rate that did not fully develop into a seismic phase which is emphasized in Figure 7b. This feature corresponds to the emergence of sub-surface events, in which the rupture does not propagate all the way to the free surface. As a result, this event causes an increase in the shear stress and slip rate at the free surface, but is still lower than the background plate loading and seismic slip rate. In the following discussion we will use the term "surface reaching event" to describe an event in which the rupture propagates all the way to the free surface, while "sub-surface events" will be used to describe those that do not reach the free surface.

Figure 8 shows the cumulative slip profile with different earthquake sequence patterns for three cases of LVFZ with different widths  $W$ . The blue solid lines are plotted every five years and show the inter-seismic creep starting in the velocity-strengthening region and penetrating into the velocity-weakening region. The quasi-dynamic rupture is shown with dashed red lines and plotted every one second. Figure 8a shows the sub-surface events that fail to propagate to the free surface. Furthermore, we observe a significant slip accumulation during the subsequent surface reaching event. This is due to the slip deficit that accumulates at the surface from the sub-surface ruptures which is compensated for by the increased slip in the subsequent surface reaching event.

Figure 8b shows the earthquake sequence for a case with  $W/h^* = 0.65$ , resulting in periodic successive surface reaching events. Interestingly, in this case, the rupture decelerates over

562 the deeper half of the fault and then appears to accelerate again. This is further discussed in  
 563 Appendix A. The limit of a homogeneous case with  $\mu = 19.8$  GPa is demonstrated in Figure  
 564 8c, where sub-surface events are followed by surface reaching ones.

565 Figure 9a shows the peak slip rate as a function of time for a number of cases correspond-  
 566 ing to different normalized widths of the LVFZ. Most notably, the sequence of events suggests  
 567 non-monotonic complex patterns as the width of the LVFZ increases. On one hand, for a small  
 568 width  $W/h^* = 0.04$ , the pattern is periodic and the inter-event time is uniform. On the other  
 569 hand, if the width of the LVFZ is large enough ( $W/h^* = \infty$ ), the sequence converges to a re-  
 570 peating pattern of alternating surface reaching and sub-surface events. Bridging the two lim-  
 571 its, for intermediate widths of the LVFZ  $W/h^* = 0.09$  (as shown in Figure 7b), the long-term  
 572 response converge to a pattern of two surface reaching events, and a subsequent sub-surface event.  
 573 The sub-surface event is characterized by a front that emerges in the VW region with the same  
 574 nucleation size as the other events; yet since it never reaches the free surface, the maximum slip  
 575 rate is not as large as the surface reaching events. It is also observed that following a sub-surface  
 576 event, the subsequent surface reaching event is delayed. We note that (Lapusta & Rice, 2003)  
 577 reported a similar observation of sub-surface events, or partial ruptures, due to the reduction  
 578 of nucleation size, which in our case is attributed to the inclusion of LVFZ. However, we note  
 579 that for some cases with  $0.62 < W/h^* \leq 1$ , as demonstrated in Figure 9b, in which the nu-  
 580 cleation size did in fact decrease, sub-surface events did not emerge. This indicates that the nu-  
 581 cleation size is not the sole contributor to the emergence and, in this case, the suppression of  
 582 sub-surface event.

583 Figure 10 summarizes how the peak slip rate and the inter-event time vary as a function  
 584 of the normalized widths for the different patterns investigated in this study. As discussed pre-  
 585 viously for the case of mild rigidity contrast, the general trend is that the peak slip rate increases  
 586 as the width of the low-velocity zone increases as shown in Figure 10a. However, unlike the case  
 587 of mild rigidity contrast, there is a considerable complexity in the inter-event time pattern. There  
 588 is a transition from a single period at small widths, to triple periods at intermediate widths,  
 589 to single periods as the width is further increased, and eventually settling into a double period  
 590 pattern in the limit of homogeneous medium with a shear modulus equal to that of the LVFZ.  
 591 As discussed previously, some of the events in the more complex sequences stop before reach-  
 592 ing the surface and thus events within these periodic clusters are not identical. Furthermore,  
 593 we observe that the general trend of increasing peak slip rate is not observed in cases with larger  
 594 LVFZ width  $W/h^* = 0.65-1$ . Since these events are associated with successive surface reach-  
 595 ing events, this deviation emerge due to the lack of residual stress concentration from a pre-  
 596 ceding sub-surface event. Thus, the peak slip rate values are lower than intermediate LVFZ cases  
 597 with  $W/h^* = 0.1 - 0.45$  where sub-surface events are observed, but still higher than in the  
 598 homogeneous case.

599 To gain further insights into the characteristics of these alternating surface reaching and  
 600 sub-surface events, we investigate the spatio-temporal evolution of the fault shear stress. Fig-  
 601 ure 11 shows snapshots of the shear stress  $\tau$  along the fault surface before, during, and after  
 602 both types of events for the case with  $W/h^* = 0.09$ . Prior to either event there is only stress  
 603 concentration due to the inter-seismic slip backing beyond the VS-VW transition region into  
 604 the VW region. Figure 11b shows that the event nucleates behind the region with stress con-  
 605 centration. The nucleation size is about  $h^* = 1.54$ km which is in line with the estimated size  
 606 of  $h_{est}^* = 1.51$  km from expression (40), indicating that both small and surface reaching events  
 607 have approximately the same nucleation size.

608 The instability results in two propagating fronts, one expanding in the direction of the  
 609 free surface and the other in the direction of the VS region with the VS region acting as a bar-  
 610 rier to the rupture as shown in Figure 11c-f. Figure 11g shows that in the case of the sub-surface  
 611 event the expanding rupture slows down as it propagates further in the VW region till it finally  
 612 arrests before reaching the free surface. However, this premature arrest results in a residual stress  
 613 concentration in the arrest region that would facilitate the propagation of subsequent surface  
 614 reaching events as demonstrated by the stress profile 10 years after the sub-surface event in Fig-  
 615 ure 11h. The sub-surface event results in a lower average shear stress below the arrest region  
 616 between 7–14 km, explaining why following the sub-surface event, a delay in the occurrence  
 617 of the next surface reaching event is observed.

618 The nucleation process for both the sub-surface and surface reaching events is illustrated  
 619 in Figures 12a-b, which shows the slip rate versus the depth normalized by the estimated nu-  
 620 cleation size. The nucleation size observed numerically is in excellent agreement with the the-  
 621 oretical estimate from expression (40) and is similar for both events. There exists some minor  
 622 variation in the detailed distribution of the slip rate within the nucleation profile but the over-  
 623 all pattern is the same. The evolution of the peak slip rate in Figure 12c suggests that the sur-  
 624 face reaching event experiences a slower increase in the peak slip rate and a slightly longer time  
 625 to instability during the nucleation process.

### 626 **3.2.3 Strong Rigidity Contrast: $\mu_D/\mu = 0.4$**

627 Figure 13a shows the surface slip rate as a function of time, demonstrating that the com-  
 628 plexity observed in Section 3.2.2 still occurs for the larger material contrast. In particular, we  
 629 still observe for some cases a kink in the surface slip rate profile that represents a slight increase  
 630 in slip rate which did not fully develop into a seismic phase (as shown in Figure 13b). This  
 631 feature corresponds to the emergence of sub-surface events, in which the rupture does not prop-  
 632 agate all the way to the free surface. Furthermore, for the cases considered, the sequence of events  
 633 follows a non-monotonic complex pattern.

634 Figure 14 elaborates further on this non-monotonicity. Figure 14a shows that initially at  
 635 smaller  $W/h^*$  the response is composed of periodic clusters of three events: two surface reach-  
 636 ing events with a sub-surface event in between. However, when the  $W/h^*$  increases and the do-  
 637 main becomes more compliant, the behavior shifts to a single surface reaching event and a sub-  
 638 surface event as illustrated in Figures 14b-c. At an intermediate  $W/h^* = 0.7$  (shown in Fig-  
 639 ure 14d), a single periodic event is observed with only surface reaching events. At large width  
 640  $W/h^* = 1.5$ , the steady state response consists of clusters of two events: one surface reach-  
 641 ing and one sub-surface but with different inter-event times compared to Figures 14b-c. We note  
 642 that different models take different times to lose their memory of the initial conditions until they  
 643 reach the statistical steady-state discussed here. Figure 14(a-d) shows small perturbation in the  
 644 slip rate that manifest during inter-seismic period, yet fails to produce an instability. These tran-  
 645 sient accelerations in aseismic slip will be a focus of future investigations.

646 Figure 15 summarizes the main characteristics of the sequence of events. The overall arch-  
 647 ing slip rate amplification is still observed (as shown in Figure 15a), except for the case of  $W/h^* =$   
 648  $0.7$ . While for this case the slip rate is still higher than in the homogeneous case, the slip rate  
 649 is slightly lower than the values observed at a lower LVFZ width. Since the sequence of events  
 650 for this specific case consist of successive surface reaching events, this discrepancy may be at-  
 651 tributed to the lack of residual stress concentration from sub-surface events that would yield  
 652 a higher slip rate in the surface reaching events. In regards to the inter-event time shown in  
 653 Figure 15b we observe a complex pattern. There is a transition from single-period events, to  
 654 triple period events, to double periods then single periods again. Eventually double period events  
 655 emerge as the width of the LVFZ goes to infinity. Interestingly, we also observe consistently that  
 656 the inter-event time between the sub-surface event and the surface reaching event shrinks as  
 657  $W/h^*$  increase. However, the inter-event time between the surface reaching event and the sub-  
 658 sequent sub-surface event increases as  $W/h^*$  increase. If we consider the cases of two surface  
 659 reaching events between  $\mu_D/\mu = 0.4$  and  $\mu_D/\mu = 0.6$ , the inter-event times fall within the  
 660 same range even though  $W/h^*$  is smaller.

## 661 **4 Discussion**

662 In this paper, we have proposed a computational framework for modeling the quasi-dynamic  
 663 sequence of earthquake and aseismic slip in an accurate and computationally efficient way with-  
 664 out the need to fully discretize the entire domain of the problem. Specifically, we have intro-  
 665 duced a hybrid scheme, coupling the finite element method (FEM) and the spectral boundary  
 666 integral (SBI) method in a 2-D anti-plane setting. The proposed framework is capable of sim-  
 667 ulating the long-term history of seismic and aseismic slip on a vertical fault embedded in a het-  
 668 erogeneous medium with a free surface. Our approach resolves the various temporal scales as-  
 669 sociated with the inter-seismic slip and instability nucleation, dynamic rupture propagation,  
 670 and post-seismic relaxation. During the dynamic rupture, the inertia terms were approximated

671 using a radiation damping term (Rice, 1993). We then verified the proposed approach using  
 672 the SCEC SEAS BP-1 benchmark (Erickson & Jiang, 2018), revealing an excellent agreement  
 673 between the proposed technique and the well-established pure SBI approach. Furthermore, we  
 674 demonstrated that the accuracy of the solution is independent of the FEM domain thickness,  
 675 due to the exact nature of the truncation of the elastic fields being provided by the SBI for-  
 676 mulation. Using the verified formulation, we investigated the evolutionary dynamics of a ver-  
 677 tically dipping fault embedded in a low-velocity fault zone (LVFZ) of varying thickness and bulk  
 678 properties.

679 A main advantage of the proposed approach is the ability of domain truncation, while re-  
 680 taining the independence of solution from the far-field boundary condition; thus, the solution  
 681 is impartial to the FEM domain dimension. This allows for a reduction in the spatial discretiza-  
 682 tion of the full domain to a small area of interest. The reduction in size translates to a small  
 683 system of equations for bulk displacement, yielding significant reduction in the computational  
 684 cost. The small linear system can be efficiently solved using direct solvers, circumventing the  
 685 need for the choice of a proper preconditioner (Heinecke et al., 2014), which is a computational  
 686 bottleneck when it comes to solving this class of problems using a purely domain based approach.  
 687 Along the same lines, further mesh refinement is possible without the scaling complexities as-  
 688 sociated with a bigger domain; thus, allowing for explicit representation of extreme heterogeneities  
 689 and potential other bulk nonlinearities with high resolution. Furthermore, the hybrid scheme  
 690 utilizes a spectral representation of the boundary integral scheme to transform the non-local  
 691 boundary conditions in space to local ones in the Fourier domain. This account for further com-  
 692 putational savings. The truncation of the domain in the hybrid scheme accounts for savings in  
 693 the overall run time, as well as memory utilization, as demonstrated in earlier studies (Ma et  
 694 al., 2018). It is noted that the correction steps involved in the proposed algorithm incur ad-  
 695 ditional computation cost; however, the cost is far less than the cost associated with modeling  
 696 the entire domain.

697 Field observations have shown that faults are usually embedded in LVZs, in which the fault  
 698 is surrounded by damaged rocks that are softer than the host rock material. LVFZs are usu-  
 699 ally several hundreds of meters wide, and may have significant reduction in seismic wave ve-  
 700 locities (Yang & Zhu, 2010; Li et al., 1994). Several studies have considered LVFZ in terms of  
 701 theoretical investigations of rupture nucleation (Ampuero et al., 2002), and computational mod-  
 702 eling of dynamic ruptures (Brietzke & Ben-Zion, 2006; Ben-Zion & Huang, 2002), but few have  
 703 considered the problem of modeling earthquake cycles in the presence of this class of bulk het-  
 704 erogeneity. (Huang & Ampuero, 2011) have demonstrated the role the LVFZ plays during a sin-  
 705 gular dynamic rupture event showing pulse like rupture. (Ma & Elbanna, 2015) showed that near  
 706 fault low-velocity elastic inclusions alters the conditions for supershear propagation enabling  
 707 supershear ruptures to occur at a much lower stress than required in homogeneous media. (Kaneko  
 708 et al., 2011) developed an alternating quasistatic-dynamic scheme and focused on earthquake  
 709 cycle simulation for faults embedded within a LVFZ. However, the study was limited to sequence  
 710 of small repeating earthquakes, within a smaller scale problem considering only one level of ma-  
 711 terial contrast between the LVFZ and the surrounding host rock. In our investigation, despite  
 712 focusing on quasi-dynamic simulations, we have taken advantage of the hybrid scheme to study  
 713 a larger length scale with a wider variety of material properties.

714 Our investigation for the low-velocity fault zone has revealed several interesting charac-  
 715 teristics. For example, at small LVFZ material contrast  $\mu_D/\mu = 0.8$ , it was observed that the  
 716 peak slip rate for successive events would increase with the increase of the normalized width  
 717 of the low-velocity zone  $W/h^*$ . We have also observed that at larger widths of the LVZ, the time  
 718 between subsequent events increase. Both observations are consistent with results from (Kaneko  
 719 et al., 2011), suggesting that they are intrinsic in the nature of the LVZ and less sensitive to  
 720 the inertia effects during dynamic rupture. Furthermore, in the quasi-dynamic limit considered  
 721 here, and at larger material contrast, our results indicate the emergence of alternating sub-surface  
 722 and surface reaching events. These sub-surface events contribute to a delay in the occurrence  
 723 of the following surface reaching event. These results are in line with some field observations  
 724 in which earthquakes fail to penetrate the Earth surface (Hartzell & Heaton, 1983).

725 Moreover, the earthquake cycle complexity in which sub-surface events emerge is shown  
 726 to be directly correlated to the compliance of the LVFZ. The study of the nucleation process

727 for both surface reaching and sub-surface events demonstrated that the nucleation size of both  
 728 events is very similar. However, we observed some minor variation in terms of depth and slip  
 729 rate profile. This observation is consistent with findings in (Lapusta & Rice, 2003), which sug-  
 730 gested the emergence of small event complexity in a homogeneous medium as the length scale  
 731 parameter in the rate and state friction law decreases, leading to a reduction in the nucleation  
 732 size, but stated that both large and small events have similar nucleation characteristics. While  
 733 the effective nucleation size decreases due to the introduction of a LVFZ, our findings suggest  
 734 that the nucleation size is not entirely the determining factor as such complexity is not obvi-  
 735 ous for cases with the same  $W/h^*$  but different rigidity contrast. If the nucleation size was the  
 736 only factor, we would expect the greatest complexity to emerge in the case of  $W \rightarrow \infty$  which  
 737 has the smallest nucleation size. However, we observe that LVFZ with small to intermediate  
 738  $W/h^*$  ratios may show a richer behavior indicating that the rigidity contrast plays a critical  
 739 role in promoting complexity, in addition to the reduced nucleation size. Furthermore, while  
 740 sub-surface and surface reaching events do appear in the limit of  $W/h^* \rightarrow \infty$ , the sequence  
 741 pattern is completely different than in the intermediate thickness cases.

742 Within a specific parameter space, it is observed that the sequence of earthquakes may  
 743 vary drastically, from a sequence of single periodic events to a pattern of repeating event clus-  
 744 ters. The pattern may be either a sequence of one sub-surface event followed by a surface reach-  
 745 ing event or one sub-surface event followed by two surface reaching events. The pattern of events  
 746 also follows a non-monotonic trend. For example, at  $\mu_D/\mu = 0.6$  we observe that at low  $W/h^*$ ,  
 747 the sequence of events start as single successive events. However, with the increase of  $W/h^*$ ,  
 748 the pattern shifts to a triple-event cluster. Finally, at  $W = \infty$ , the pattern converge to a clus-  
 749 ter of two events. Overall, we found that the introduction of LVFZ contribute to an increase  
 750 in the maximum peak slip rate within the earthquake sequence particularly as the rigidity con-  
 751 trast increases. The peak slip rate generally increases with respect to the homogeneous host  
 752 rock case as the width of the LVFZ increases, with some minor fluctuations depending on the  
 753 details of the seismic sequence.

754 While the proposed hybrid scheme offers a step toward computationally efficient and ac-  
 755 curate methodologies for including fault zone complexities within earthquake cycle simulations,  
 756 the method as presented here has some limitations. Most notably, in the proposed scheme we  
 757 have opted to disregard the inertia terms and instead employ the radiation damping approx-  
 758 imation. While this approach gives grave insight on the nucleation and inter-seismic response  
 759 of the earthquake cycle, it lacks in consideration the substantial role of inertia during the dy-  
 760 namic rupture process. The radiation damping correction used here only approximates this in-  
 761 ertia effect, but it was shown previously, at least in the framework of planar faults in homo-  
 762 geneous media, that some differences in the characteristics of earthquake sequence may be ob-  
 763 served between dynamic and quasi-dynamic simulations (Thomas et al., 2014). Furthermore,  
 764 in a fully dynamic framework, the incorporation of a damaged zone will result in wave reflec-  
 765 tion and trapped seismic waves (Y.-G. Li & Leary, 1990). The quasi-dynamic approximation  
 766 will fail to capture the role of reflected waves and its impact on SEAS. (Hajarolasvadi & El-  
 767 banna, 2017) and (Ma et al., 2018) have considered dynamics within the same hybrid frame-  
 768 work for a single dynamic rupture event and demonstrated that the results obtained match per-  
 769 fectly with FEM within anti-plane and in-plane 2-D settings but at a fraction of computational  
 770 cost. Thus, the next natural step for the current SEAS implementation would be to extend it  
 771 to include inertial dynamics. This will be further explored in future investigations.

772 It should be noted that even though we are using a quasi-dynamic approximation, sev-  
 773 eral other studies indicate that some of the features observed in the current models mimic those  
 774 happening in a fully dynamic simulation. For example, (Lapusta et al., 2000) demonstrated that  
 775 sequence of small and large events would still occur in dynamic systems with small nucleation  
 776 size. A more relevant observation to the quasi-dynamic limit that is common between this cur-  
 777 rent study and (Lapusta & Rice, 2003) is that the nucleation process for both small and large  
 778 events is similar. Similarly, (Kaneko et al., 2011) also demonstrated that amplification in the  
 779 slip rate and increase in inter-event time is proportional to  $W/h^*$  for  $\mu_D/\mu = 0.6$  within a dy-  
 780 namic framework for the co-seismic phase, which is also observed in the current study.

781 In this work, we have focused on modeling planar faults as an initial step. However, the  
 782 hybrid scheme can fully accommodate non-planar fault setups, as well as other complex fault

783 zone topologies including fault branches (Ma & Elbanna, 2019). Furthermore, the Galerkin fi-  
 784 nite element approach used in the current study may be replaced by any other domain-based  
 785 model. For example, if we want to relax the constraint that the fault location is known a pri-  
 786 ori, a more flexible approach would be to adopt a discretization approach that readily accounts  
 787 for discontinuities such as generalized finite element method (F. Liu & Borja, 2009), or discon-  
 788 tinuous Galerkin methods (Pelties et al., 2012), or phase field model (Miehe et al., 2010), which  
 789 would further enable arbitrary growth of fault surfaces, as well as nucleation and growth of new  
 790 surfaces. Furthermore, the FEM may be replaced by a discrete element method (Herrmann et  
 791 al., 1998) or smooth particle hydrodynamics formulation (Bui et al., 2008) to enable explicit  
 792 incorporation of fault gouge dynamics. The proposed hybrid scheme is general enough to work  
 793 with any of those approaches, and we plan to explore these implementation in the future.

794 In this paper, we have limited our investigation to modeling sequence of earthquakes and  
 795 aseismic slip in linearly elastic heterogeneous domains undergoing anti-plane deformations. How-  
 796 ever, as demonstrated in (Hajarolasvadi & Elbanna, 2017) and (Ma et al., 2018) the hybrid scheme  
 797 may be readily extended to account for nonlinear bulk rheology as well as 2-D in-plane setting  
 798 with complex fault topology. Extension to 3-D setups with nonlinear constitutive laws is also  
 799 straightforward. By enlarging the scope of our investigations to these new directions, this would  
 800 potentially provide more insight on the role of various forms of fault zone complexities, includ-  
 801 ing topological, geometrical, and rheological nonlinearities, on the spatio-temporal evolution  
 802 of seismicity.

803 While in the current study we have demonstrated that the compliant zone plays an im-  
 804 portant role in altering the earthquake sequence, our future effort would involve a more exten-  
 805 sive parametric study to evaluate the nature of the transition of the earthquake patterns with  
 806 respect to LVFZ parameters and to explore the possible emergence of chaotic patterns. Fur-  
 807 thermore, we have chosen to vary the LVFZ width and rigidity while keeping fault parameters  
 808 fixed. We recognize that the interplay between the fault properties, such as the velocity-weakening  
 809 length  $H$  and the critical slip distance  $L$ , would warrant future investigation.

## 810 5 Conclusion

811 In this paper, we present a hybrid framework that couples finite element method with spec-  
 812 tral boundary integral method to conduct earthquake cycle simulations, and investigate the in-  
 813 fluence of material heterogeneities on the behavior of the earthquake sequence and aseismic slip.  
 814 Such simulations incur substantial computational cost on domain based approaches, as the ma-  
 815 terial heterogeneity or nonlinearity impose restrictions on the resolution of the mesh. A ver-  
 816 ification exercise demonstrates the accuracy of the scheme, which we then utilize to study the  
 817 response of faults embedded within a low-velocity zone. The results shows the importance of  
 818 off-fault properties on the earthquake sequence. The main conclusions may be summarized as  
 819 follows:

- 820 • The proposed scheme matches other well-established numerical methods in the limit of  
 821 a homogeneous medium. This comes at a fraction of the cost that other domain-based  
 822 approaches would incur.
- 823 • The low-velocity fault zone contributes to a change in the overall properties of the earth-  
 824 quake cycle
- 825 • Should the low-velocity fault zone be sufficiently compliant, the results show the emer-  
 826 gence of sub-surface events that fail to penetrate to the free surface.
- 827 • The sub-surface and surface reaching events share similar nucleation size; however, the  
 828 sub-surface event results in a residual stress concentration that contributes to a higher  
 829 peak slip rate.
- 830 • Event pattern and LVFZ  $W/h^*$  are non-monotonously related, in which we observe tran-  
 831 sitions from single periods to triple periods, and again to single or double periods as  $W/h^*$   
 832 increase.

## Appendix A: Deceleration During Rupture

To elaborate further on the deceleration observed in Figure 8b, we show in Figure A1 the snapshots of the slip rate during one of the surface reaching events. A sharp decrease in the slip rate is observed near the VS region as the rupture propagates toward the free surface. After a few seconds, we observe a re-acceleration in this region due to another growth of instability along the fault line in Figure A1h. To further explore this phenomenon, Figure A2 shows the evolution of the slip rate along the fault depth for the time period between 33 and 39 seconds. The figure illustrates the emergence of rapid back propagating fronts associated with unstable growth of slip emanating in the vicinity of the region with steep gradient in the slip rate at the toe of the quasi-slip pulse observed in Figure A1g. Similar observations for the emergence of slip pulses and rapid back propagating fronts have been reported by (Idini & Ampuero, 2018) and warrants further investigations in the future.

## Acknowledgment

We thank Eric Dunham and Sylvain Barbot for their insightful reviews that helped improve the manuscript. We also thank Associate editor Ylona Van Dinther for her comments and input. This research has been supported by the National Science Foundation (CAREER Award Number 1753249) and the Southern California Earthquake Center through a collaborative agreement between NSF. Grant Number: EAR0529922 and USGS Grant Number: 07HQAG0008. Additional funds for investigation of low velocity fault zones were provided by the Department of Energy under Award Number DE-FE0031685. This work was prepared as an account of work sponsored by an agency of the United States Government. Neither the United States Government nor any agency thereof, nor any of their employees, makes any warranty, express or implied, or assumes any legal liability or responsibility for the accuracy, completeness, or usefulness of any information, apparatus, product, or process disclosed, or represents that its use would not infringe privately owned rights. Reference herein to any specific commercial product, process, or service by trade name, trademark, manufacturer, or otherwise does not necessarily constitute or imply its endorsement, recommendation, or favoring by the United States Government or any agency thereof. The views and opinions of authors expressed herein do not necessarily state or reflect those of the United States Government or any agency thereof. The data generated using the numerical algorithm corresponding to this study is available at <https://doi.org/10.5281/zenodo.3379091>.

## References

- Aagaard, B. T., Knepley, M. G., & Williams, C. A. (2013). A domain decomposition approach to implementing fault slip in finite-element models of quasi-static and dynamic crustal deformation. *Journal of Geophysical Research: Solid Earth*, *118*(6), 3059–3079. doi: 10.1002/jgrb.50217
- Aliabadi, M. H. (1997). Boundary Element Formulations in Fracture Mechanics. *Applied Mechanics Reviews*, *50*(2), 83. Retrieved from <http://appliedmechanicsreviews.asmedigitalcollection.asme.org/article.aspx?articleid=1395876> doi: 10.1115/1.3101690
- Allison, K. L., & Dunham, E. M. (2018). Earthquake cycle simulations with rate-and-state friction and power-law viscoelasticity. *Tectonophysics*, *733*(November 2017), 232–256. Retrieved from <https://doi.org/10.1016/j.tecto.2017.10.021> doi: 10.1016/j.tecto.2017.10.021
- Ampuero, J. P., & Ben-zion, Y. (2008). Cracks, pulses and macroscopic asymmetry of dynamic rupture on a bimaterial interface with velocity-weakening friction. *Geophysical Journal International*, *173*(2), 674–692. doi: 10.1111/j.1365-246X.2008.03736.x
- Ampuero, J.-P., & Rubin, A. M. (2008, 1). Earthquake nucleation on rate and state faults – Aging and slip laws. *Journal of Geophysical Research*, *113*(B1), B01302. Retrieved from <http://doi.wiley.com/10.1029/2007JB005082> doi: 10.1029/2007JB005082
- Ampuero, J.-P., Vilotte, J.-P., & Sánchez-Sesma, F. J. (2002, 12). Nucleation of rupture under slip dependent friction law: Simple models of fault zone. *Journal of Geophysical Research: Solid Earth*, *107*(B12), 2–1. Retrieved from <http://doi.wiley.com/10>

- 886 .1029/2001JB000452 doi: 10.1029/2001JB000452
- 887 Barbot, S. (2018). Asthenosphere Flow Modulated by Megathrust Earthquake Cycles. *Geo-*  
 888 *physical Research Letters*, *45*(12), 6018–6031. doi: 10.1029/2018GL078197
- 889 Barbot, S. (2019). Modulation of fault strength during the seismic cycle by grain-size evo-  
 890 lution around contact junctions. *Tectonophysics*, *765*(May), 129–145. Retrieved  
 891 from <https://doi.org/10.1016/j.tecto.2019.05.004> doi: 10.1016/j.tecto.2019  
 892 .05.004
- 893 Barbot, S., Fialko, Y., & Sandwell, D. (2008). Effect of a compliant fault zone on the  
 894 inferred earthquake slip distribution. *Journal of Geophysical Research: Solid Earth*,  
 895 *113*(6), 1–10. doi: 10.1029/2007JB005256
- 896 Barbot, S., Fialko, Y., & Sandwell, D. (2009). Three-dimensional models of elasto-  
 897 static deformation in heterogeneous media, with applications to the eastern cal-  
 898 ifornia shear zone. *Geophysical Journal International*, *179*(1), 500–520. doi:  
 899 10.1111/j.1365-246X.2009.04194.x
- 900 Ben-David, O., Rubinstein, S. M., & Fineberg, J. (2010). Slip-stick and the evolution of  
 901 frictional strength. *Nature*, *463*(7277), 76–79. Retrieved from [http://dx.doi.org/](http://dx.doi.org/10.1038/nature08676)  
 902 [10.1038/nature08676](http://dx.doi.org/10.1038/nature08676) doi: 10.1038/nature08676
- 903 Ben-Zion, Y., & Huang, Y. (2002). Dynamic rupture on an interface between a compli-  
 904 ant fault zone layer and a stiffer surrounding solid. *Journal of Geophysical Research*,  
 905 *107*(B2), 2042. Retrieved from <http://doi.wiley.com/10.1029/2001JB000254> doi:  
 906 10.1029/2001JB000254
- 907 Ben-Zion, Y., Peng, Z., Okaya, D., Seeber, L., Armbruster, J. G., Ozer, N., . . . Aktar,  
 908 M. (2003, 3). A shallow fault-zone structure illuminated by trapped waves in the  
 909 Karadere-Duzce branch of the North Anatolian Fault, western Turkey. *Geophys-*  
 910 *ical Journal International*, *152*(3), 699–717. Retrieved from [https://academic](https://academic.oup.com/gji/article-lookup/doi/10.1046/j.1365-246X.2003.01870.x)  
 911 [.oup.com/gji/article-lookup/doi/10.1046/j.1365-246X.2003.01870.x](https://academic.oup.com/gji/article-lookup/doi/10.1046/j.1365-246X.2003.01870.x) doi:  
 912 10.1046/j.1365-246X.2003.01870.x
- 913 Berenger, J.-p. (1994, 10). A perfectly matched layer for the absorption of electromagnetic  
 914 waves. *Journal of Computational Physics*, *114*(2), 185–200. Retrieved from [https://](https://linkinghub.elsevier.com/retrieve/pii/S0021999184711594)  
 915 [linkinghub.elsevier.com/retrieve/pii/S0021999184711594](https://linkinghub.elsevier.com/retrieve/pii/S0021999184711594) doi: 10.1006/jcph  
 916 .1994.1159
- 917 Bettess, P. (1977). Infinite elements. *International Journal for Numerical Methods*  
 918 *in Engineering*, *11*(1), 53–64. Retrieved from [http://doi.wiley.com/10.1002/nme](http://doi.wiley.com/10.1002/nme.1620110107)  
 919 [.1620110107](http://doi.wiley.com/10.1002/nme.1620110107) doi: 10.1002/nme.1620110107
- 920 Biemiller, J., & Lavier, L. (2017, 4). Earthquake supercycles as part of a spectrum of  
 921 normal fault slip styles. *Journal of Geophysical Research: Solid Earth*, *122*(4), 3221–  
 922 3240. doi: 10.1002/2016JB013666
- 923 Bizzarri, A. (2011, 8). ON THE DETERMINISTIC DESCRIPTION OF EARTH-  
 924 QUAKES. *Reviews of Geophysics*, *49*(3), RG3002. Retrieved from [http://](http://writenowmedia.com/Web_files/MathisBrothers-CompanyStory.pdf)  
 925 [writenowmedia.com/Web\\_files/MathisBrothers-CompanyStory.pdf](http://writenowmedia.com/Web_files/MathisBrothers-CompanyStory.pdf)[http://](http://doi.wiley.com/10.1029/2011RG000356)  
 926 [doi.wiley.com/10.1029/2011RG000356](http://doi.wiley.com/10.1029/2011RG000356) doi: 10.1029/2011RG000356
- 927 Breitenfeld, M. S., & Geubelle, P. H. (1998). Numerical analysis of dynamic debonding  
 928 under 2D in-plane and 3D loading. In *Recent advances in fracture mechanics* (pp. 13–  
 929 37). Dordrecht: Springer Netherlands. Retrieved from [http://link.springer.com/](http://link.springer.com/10.1007/978-94-017-2854-6_2)  
 930 [10.1007/978-94-017-2854-6\\_2](http://link.springer.com/10.1007/978-94-017-2854-6_2) doi: 10.1007/978-94-017-2854-6{\\_}2
- 931 Brietzke, G. B., & Ben-Zion, Y. (2006, 11). Examining tendencies of in-plane rupture to  
 932 migrate to material interfaces. *Geophysical Journal International*, *167*(2), 807–819.  
 933 Retrieved from [https://academic.oup.com/gji/article-lookup/doi/10.1111/](https://academic.oup.com/gji/article-lookup/doi/10.1111/j.1365-246X.2006.03137.x)  
 934 [j.1365-246X.2006.03137.x](https://academic.oup.com/gji/article-lookup/doi/10.1111/j.1365-246X.2006.03137.x) doi: 10.1111/j.1365-246X.2006.03137.x
- 935 Bui, H. H., Fukagawa, R., Sako, K., & Ohno, S. (2008, 8). Lagrangian meshfree par-  
 936 ticles method (SPH) for large deformation and failure flows of geomaterial us-  
 937 ing elastic-plastic soil constitutive model. *International Journal for Numerical*  
 938 *and Analytical Methods in Geomechanics*, *32*(12), 1537–1570. Retrieved from  
 939 <http://doi.wiley.com/10.1002/nag.688> doi: 10.1002/nag.688
- 940 Cappa, F., Perrin, C., Manighetti, I., & Delor, E. (2014, 4). Off-fault long-term damage:  
 941 A condition to account for generic, triangular earthquake slip profiles. *Geochemistry,*  
 942 *Geophysics, Geosystems*, *15*(4), 1476–1493. Retrieved from [http://doi.wiley.com/](http://doi.wiley.com/10.1002/2013GC005182)  
 943 [10.1002/2013GC005182](http://doi.wiley.com/10.1002/2013GC005182) doi: 10.1002/2013GC005182

- 944 Chester, F. M., Evans, J. P., & Biegel, R. L. (1993, 1). Internal structure and weakening  
 945 mechanisms of the San Andreas Fault. *Journal of Geophysical Research: Solid Earth*,  
 946 98(B1), 771–786. Retrieved from <http://doi.wiley.com/10.1029/92JB01866> doi:  
 947 10.1029/92JB01866
- 948 Cochard, A., & Madariaga, R. (1994). Dynamic faulting under rate-dependent  
 949 friction. *Pure and Applied Geophysics PAGEOPH*, 142(3-4), 419–445. doi:  
 950 10.1007/BF00876049
- 951 Cochard, A., & Rice, J. R. (2000, 11). Fault rupture between dissimilar materials: Ill-  
 952 posedness, regularization, and slip-pulse response. *Journal of Geophysical Research:*  
 953 *Solid Earth*, 105(B11), 25891–25907. Retrieved from [http://doi.wiley.com/](http://doi.wiley.com/10.1029/2000JB900230)  
 954 10.1029/2000JB900230 doi: 10.1029/2000JB900230
- 955 Cochran, E. S., Li, Y.-G., Shearer, P. M., Barbot, S., Fialko, Y., & Vidale, J. E. (2009,  
 956 4). Seismic and geodetic evidence for extensive, long-lived fault damage zones. *Geol-*  
 957 *ogy*, 37(4), 315–318. Retrieved from [http://pubs.geoscienceworld.org/geology/](http://pubs.geoscienceworld.org/geology/article/37/4/315/29883/Seismic-and-geodetic-evidence-for-extensive)  
 958 [article/37/4/315/29883/Seismic-and-geodetic-evidence-for-extensive](http://pubs.geoscienceworld.org/geology/article/37/4/315/29883/Seismic-and-geodetic-evidence-for-extensive) doi:  
 959 10.1130/G25306A.1
- 960 D’Amico, S. (2016). *Earthquakes and Their Impact on Society* (S. D’Amico, Ed.). Cham:  
 961 Springer International Publishing. Retrieved from [http://link.springer.com/10](http://link.springer.com/10.1007/978-3-319-21753-6)  
 962 .1007/978-3-319-21753-6 doi: 10.1007/978-3-319-21753-6
- 963 Day, S. M., Dalguer, L. A., Lapusta, N., & Liu, Y. (2005). Comparison of finite difference  
 964 and boundary integral solutions to three-dimensional spontaneous rupture. *Journal of*  
 965 *Geophysical Research: Solid Earth*, 110(12), 1–23. doi: 10.1029/2005JB003813
- 966 Dieterich, J. H. (1979). Modeling of rock friction 1. Experimental results and constitutive  
 967 equations. *Journal of Geophysical Research: Solid Earth*, 84(B5), 2161–2168. doi: 10  
 968 .1029/JB084iB05p02161
- 969 Dieterich, J. H. (1992). Earthquake nucleation on faults with rate-and state-dependent  
 970 strength. *Tectonophysics*, 211(1-4), 115–134. doi: 10.1016/0040-1951(92)90055-B
- 971 Di Toro, G., Han, R., Hirose, T., De Paola, N., Nielsen, S., Mizoguchi, K., . . . Shimamoto,  
 972 T. (2011, 3). Fault lubrication during earthquakes. *Nature*, 471(7339), 494–498. Re-  
 973 trieved from <http://dx.doi.org/10.1038/nature09838>[http://www.nature.com/](http://www.nature.com/articles/nature09838)  
 974 [articles/nature09838](http://www.nature.com/articles/nature09838) doi: 10.1038/nature09838
- 975 Dolan, J. F., & Haravitch, B. D. (2014). How well do surface slip measurements track slip  
 976 at depth in large strike-slip earthquakes? The importance of fault structural maturity  
 977 in controlling on-fault slip versus off-fault surface deformation. *Earth and Plane-*  
 978 *tary Science Letters*, 388, 38–47. Retrieved from [http://dx.doi.org/10.1016/](http://dx.doi.org/10.1016/j.epsl.2013.11.043)  
 979 [j.epsl.2013.11.043](http://dx.doi.org/10.1016/j.epsl.2013.11.043) doi: 10.1016/j.epsl.2013.11.043
- 980 Duru, K., Allison, K. L., Rivet, M., & Dunham, E. M. (2019, 7). Dynamic Rup-  
 981 ture and Earthquake Sequence Simulations Using the Wave Equation in Second-  
 982 Order Form. *Geophysical Journal International*, 1–34. Retrieved from [https://](https://academic.oup.com/gji/advance-article/doi/10.1093/gji/ggz319/5533327)  
 983 [academic.oup.com/gji/advance-article/doi/10.1093/gji/ggz319/5533327](https://academic.oup.com/gji/advance-article/doi/10.1093/gji/ggz319/5533327) doi:  
 984 10.1093/gji/ggz319
- 985 Erickson, B. A., & Day, S. M. (2016). Journal of Geophysical Research : Solid Earth Bima-  
 986 terial effects in an earthquake cycle model using rate-and-state friction. , 2480–2506.  
 987 doi: 10.1002/2015JB012470.Received
- 988 Erickson, B. A., & Dunham, E. M. (2014). An efficient numerical method for earthquake  
 989 cycles in heterogeneous media: Alternating subbasin and surface-rupturing events on  
 990 faults crossing a sedimentary basin. *Journal of Geophysical Research: Solid Earth*,  
 991 119(4), 3290–3316. doi: 10.1002/2013JB010614
- 992 Erickson, B. A., Dunham, E. M., & Khosravifar, A. (2017). A finite difference method  
 993 for off-fault plasticity throughout the earthquake cycle. *Journal of the Mechanics and*  
 994 *Physics of Solids*, 109, 50–77. Retrieved from [http://dx.doi.org/10.1016/j.jmps](http://dx.doi.org/10.1016/j.jmps.2017.08.002)  
 995 .2017.08.002 doi: 10.1016/j.jmps.2017.08.002
- 996 Erickson, B. A., & Jiang, J. (2018). *SEAS Benchmark Problem BP1*. Retrieved from  
 997 <http://scecddata.usc.edu/cvws/seas/>
- 998 Geubelle, P., & Rice, J. R. (1995, 11). A spectral method for three-dimensional elastody-  
 999 namic fracture problems. *Journal of the Mechanics and Physics of Solids*, 43(11),  
 1000 1791–1824. Retrieved from [https://linkinghub.elsevier.com/retrieve/pii/](https://linkinghub.elsevier.com/retrieve/pii/S002250969500043I)  
 1001 002250969500043I doi: 10.1016/0022-5096(95)00043-I

- 1002 Geubelle, P. H., & Breitenfeld, M. S. (1997). Numerical analysis of dynamic debonding under  
1003 anti-plane shear loading. *International Journal of Fracture*, *85*(3), 265–282. doi:  
1004 <https://doi.org/10.1023/A:1007498300031>
- 1005 Goldsby, D. L., & Tullis, T. E. (2011, 10). Flash Heating Leads to Low Frictional Strength  
1006 of Crustal Rocks at Earthquake Slip Rates. *Science*, *334*(6053), 216–218. Retrieved  
1007 from <http://www.sciencemag.org/cgi/doi/10.1126/science.1207902> doi:  
1008 10.1126/science.1207902
- 1009 Hajarolasvadi, S., & Elbanna, A. E. (2017, 11). A new hybrid numerical scheme  
1010 for modelling elastodynamics in unbounded media with near-source hetero-  
1011 geneities. *Geophysical Journal International*, *211*(2), 851–864. Retrieved from  
1012 [http://academic.oup.com/gji/article/211/2/851/4082246/A-new-hybrid-](http://academic.oup.com/gji/article/211/2/851/4082246/A-new-hybrid-numerical-scheme-for-modelling)  
1013 [numerical-scheme-for-modelling](http://academic.oup.com/gji/article/211/2/851/4082246/A-new-hybrid-numerical-scheme-for-modelling) doi: 10.1093/gji/ggx337
- 1014 Hartzell, S., & Heaton, T. (1983). Inversion of strong ground motion and teleseismic  
1015 waveform data for the fault rupture history of the 1979 Imperial Valley, California,  
1016 earthquake. *Bulletin of the Seismological Society of ...*, *73*(6), 1553–1583. Retrieved  
1017 from <http://www.bssaonline.org/content/73/6A/1553.short>
- 1018 Heinecke, A., Breuer, A., Rettenberger, S., Bader, M., Gabriel, A.-A., Pelties, C., ...  
1019 Dubey, P. (2014, 11). Petascale High Order Dynamic Rupture Earthquake Sim-  
1020 ulations on Heterogeneous Supercomputers. In *Sci14: International conference for*  
1021 *high performance computing, networking, storage and analysis* (Vol. 2015-Janua, pp.  
1022 3–14). IEEE. Retrieved from <http://ieeexplore.ieee.org/document/7012188/>  
1023 doi: 10.1109/SC.2014.6
- 1024 Herrendörfer, R., Gerya, T., & van Dinther, Y. (2018, 6). An Invariant Rate- and State-  
1025 Dependent Friction Formulation for Viscoelastoplastic Earthquake Cycle Simula-  
1026 tions. *Journal of Geophysical Research: Solid Earth*, *123*(6), 5018–5051. doi:  
1027 10.1029/2017JB015225
- 1028 Herrmann, H. J., Hovi, J.-P., & Luding, S. (Eds.). (1998). *Physics of Dry Granular Me-*  
1029 *dia*. Dordrecht: Springer Netherlands. Retrieved from [http://link.springer.com/](http://link.springer.com/10.1007/978-94-017-2653-5)  
1030 [10.1007/978-94-017-2653-5](http://link.springer.com/10.1007/978-94-017-2653-5) doi: 10.1007/978-94-017-2653-5
- 1031 Hillers, G., Ben-Zion, Y., & Mai, P. M. (2006). Seismicity on a fault controlled by rate-  
1032 and state-dependent friction with spatial variations of the critical slip distance. *Jour-*  
1033 *nal of Geophysical Research: Solid Earth*, *111*(1), 1–23. doi: 10.1029/2005JB003859
- 1034 Huang, Y., & Ampuero, J.-P. (2011, 12). Pulse-like ruptures induced by low-velocity fault  
1035 zones. *Journal of Geophysical Research*, *116*(B12), B12307. Retrieved from [http://](http://doi.wiley.com/10.1029/2011JB008684)  
1036 [doi.wiley.com/10.1029/2011JB008684](http://doi.wiley.com/10.1029/2011JB008684) doi: 10.1029/2011JB008684
- 1037 Huang, Y., Ampuero, J.-P., & Helmberger, D. V. (2014, 4). Earthquake ruptures modu-  
1038 lated by waves in damaged fault zones. *Journal of Geophysical Research: Solid Earth*,  
1039 *119*(4), 3133–3154. Retrieved from <http://doi.wiley.com/10.1002/2013JB010724>  
1040 doi: 10.1002/2013JB010724
- 1041 Huang, Y., Beroza, G. C., & Ellsworth, W. L. (2016, 9). Stress drop estimates of poten-  
1042 tially induced earthquakes in the Guy-Greenbrier sequence. *Journal of Geophysical*  
1043 *Research: Solid Earth*, *121*(9), 6597–6607. Retrieved from [http://doi.wiley.com/](http://doi.wiley.com/10.1002/2016JB013067)  
1044 [10.1002/2016JB013067](http://doi.wiley.com/10.1002/2016JB013067) doi: 10.1002/2016JB013067
- 1045 Idini, B. R., & Ampuero, J.-p. (2018). Rupture Complexity Promoted by Dam-  
1046 aged Fault Zones in Earthquake Cycle Models. , *110*(2011), 10500080. doi:  
1047 10.5281/zen-odo.322459
- 1048 Kaneko, Y., Ampuero, J.-P., & Lapusta, N. (2011, 10). Spectral-element simulations of  
1049 long-term fault slip: Effect of low-rigidity layers on earthquake-cycle dynamics. *Jour-*  
1050 *nal of Geophysical Research*, *116*(B10), B10313. Retrieved from [http://doi.wiley](http://doi.wiley.com/10.1029/2011JB008395)  
1051 [.com/10.1029/2011JB008395](http://doi.wiley.com/10.1029/2011JB008395) doi: 10.1029/2011JB008395
- 1052 Kaneko, Y., Lapusta, N., & Ampuero, J.-P. (2008, 9). Spectral element modeling  
1053 of spontaneous earthquake rupture on rate and state faults: Effect of velocity-  
1054 strengthening friction at shallow depths. *Journal of Geophysical Research*, *113*(B9),  
1055 B09317. Retrieved from <http://doi.wiley.com/10.1029/2007JB005553> doi:  
1056 10.1029/2007JB005553
- 1057 Kuna, M. (2013). *Finite Elements in Fracture Mechanics* (Vol. 201). Dordrecht:  
1058 Springer Netherlands. Retrieved from [http://link.springer.com/10.1007/](http://link.springer.com/10.1007/978-94-007-6680-8)  
1059 [978-94-007-6680-8](http://link.springer.com/10.1007/978-94-007-6680-8) doi: 10.1007/978-94-007-6680-8

- 1060 Lapusta, N., & Liu, Y. (2009). Three-dimensional boundary integral modeling of sponta-  
 1061 neous earthquake sequences and aseismic slip. *Journal of Geophysical Research: Solid*  
 1062 *Earth*, *114*(9), 1–25. doi: 10.1029/2008JB005934
- 1063 Lapusta, N., & Rice, J. R. (2003, 4). Nucleation and early seismic propagation of small  
 1064 and large events in a crustal earthquake model. *Journal of Geophysical Research:*  
 1065 *Solid Earth*, *108*(B4), 1–18. Retrieved from [http://doi.wiley.com/10.1029/](http://doi.wiley.com/10.1029/2001JB000793)  
 1066 [2001JB000793](http://doi.wiley.com/10.1029/2001JB000793) doi: 10.1029/2001JB000793
- 1067 Lapusta, N., Rice, J. R., Ben-Zion, Y., & Zheng, G. (2000, 10). Elastodynamic analysis  
 1068 for slow tectonic loading with spontaneous rupture episodes on faults with rate- and  
 1069 state-dependent friction. *Journal of Geophysical Research: Solid Earth*, *105*(B10),  
 1070 23765–23789. Retrieved from <http://doi.wiley.com/10.1029/2000JB900250> doi:  
 1071 [10.1029/2000JB900250](http://doi.wiley.com/10.1029/2000JB900250)
- 1072 Lay, T. (2012). Seismology: Why giant earthquakes keep catching us out. *Nature*,  
 1073 *483*(7388), 149–150. doi: 10.1038/483149a
- 1074 Lewis, M. A., & Ben-Zion, Y. (2010, 12). Diversity of fault zone damage and trapping  
 1075 structures in the Parkfield section of the San Andreas Fault from comprehensive anal-  
 1076 ysis of near fault seismograms. *Geophysical Journal International*, *183*(3), 1579–1595.  
 1077 Retrieved from [https://academic.oup.com/gji/article-lookup/doi/10.1111/](https://academic.oup.com/gji/article-lookup/doi/10.1111/j.1365-246X.2010.04816.x)  
 1078 [j.1365-246X.2010.04816.x](https://academic.oup.com/gji/article-lookup/doi/10.1111/j.1365-246X.2010.04816.x) doi: 10.1111/j.1365-246X.2010.04816.x
- 1079 Li, Y.-G., Aki, K., Adams, D., Hasemi, A., & Lee, W. H. K. (1994, 6). Seismic guided  
 1080 waves trapped in the fault zone of the Landers, California, earthquake of 1992. *Jour-*  
 1081 *nal of Geophysical Research: Solid Earth*, *99*(B6), 11705–11722. Retrieved from  
 1082 <http://doi.wiley.com/10.1029/94JB00464> doi: 10.1029/94JB00464
- 1083 Lindsey, E. O., Sahakian, V. J., Fialko, Y., Bock, Y., Barbot, S., & Rockwell, T. K. (2014).  
 1084 Interseismic Strain Localization in the San Jacinto Fault Zone. *Pure and Applied*  
 1085 *Geophysics*, *171*(11), 2937–2954. doi: 10.1007/s00024-013-0753-z
- 1086 Liu, F., & Borja, R. I. (2009, 9). An extended finite element framework for slow-rate fric-  
 1087 tional faulting with bulk plasticity and variable friction. *International Journal for*  
 1088 *Numerical and Analytical Methods in Geomechanics*, *33*(13), 1535–1560. Retrieved  
 1089 from <http://doi.wiley.com/10.1002/nag.777> doi: 10.1002/nag.777
- 1090 Liu, Y., & Rice, J. R. (2007, 9). Spontaneous and triggered aseismic deformation tran-  
 1091 sients in a subduction fault model. *Journal of Geophysical Research*, *112*(B9),  
 1092 B09404. Retrieved from <http://doi.wiley.com/10.1029/2007JB004930> doi:  
 1093 [10.1029/2007JB004930](http://doi.wiley.com/10.1029/2007JB004930)
- 1094 Luo, Y., & Ampuero, J.-P. (2018, 5). Stability of faults with heterogeneous friction  
 1095 properties and effective normal stress. *Tectonophysics*, *733*(October 2017), 257–  
 1096 272. Retrieved from <https://doi.org/10.1016/j.tecto.2017.11.006>[https://](https://linkinghub.elsevier.com/retrieve/pii/S0040195117304596)  
 1097 [linkinghub.elsevier.com/retrieve/pii/S0040195117304596](https://linkinghub.elsevier.com/retrieve/pii/S0040195117304596) doi: 10.1016/  
 1098 [j.tecto.2017.11.006](https://linkinghub.elsevier.com/retrieve/pii/S0040195117304596)
- 1099 Lyakhovskiy, V., Ben-Zion, Y., Ilchev, A., & Mendecki, A. (2016, 8). Dynamic rupture  
 1100 in a damage-breakage rheology model. *Geophysical Journal International*, *206*(2),  
 1101 1126–1143. Retrieved from [https://academic.oup.com/gji/article-lookup/doi/](https://academic.oup.com/gji/article-lookup/doi/10.1093/gji/ggw183)  
 1102 [10.1093/gji/ggw183](https://academic.oup.com/gji/article-lookup/doi/10.1093/gji/ggw183) doi: 10.1093/gji/ggw183
- 1103 Lysmer, O., & Kuhlemeyer, R. L. (1969). Finite Dynamic Model for Infinite Media. *Jour-*  
 1104 *nal of the Engineering Mechanics Division, ASCE*, *95*(8), 859–869.
- 1105 Ma, X., & Elbanna, A. (2015, 10). Effect of off-fault low-velocity elastic inclusions on  
 1106 supershear rupture dynamics. *Geophysical Journal International*, *203*(1), 664–677.  
 1107 Retrieved from [https://academic.oup.com/gji/article-lookup/doi/10.1093/](https://academic.oup.com/gji/article-lookup/doi/10.1093/gji/ggv302)  
 1108 [gji/ggv302](https://academic.oup.com/gji/article-lookup/doi/10.1093/gji/ggv302) doi: 10.1093/gji/ggv302
- 1109 Ma, X., & Elbanna, A. E. (2019). Dynamic Rupture Propagation on Fault Planes with  
 1110 Explicit Representation of Short Branches Dynamic Rupture Propagation on Fault  
 1111 Planes with Explicit Representation of Short Branches. *EarthArXiv*.
- 1112 Ma, X., Hajarolasvadi, S., Albertini, G., Kammer, D. S., & Elbanna, A. E. (2018, 1).  
 1113 A hybrid finite element-spectral boundary integral approach: Applications to dy-  
 1114 namic rupture modeling in unbounded domains. *International Journal for Nu-*  
 1115 *merical and Analytical Methods in Geomechanics*, *43*(1), 317–338. Retrieved  
 1116 from <https://onlinelibrary.wiley.com/doi/abs/10.1002/nag.2865> doi:  
 1117 [10.1002/nag.2865](https://onlinelibrary.wiley.com/doi/abs/10.1002/nag.2865)

- 1118 Miehe, C., Welschinger, F., & Hofacker, M. (2010, 9). Thermodynamically consistent  
 1119 phase-field models of fracture: Variational principles and multi-field FE implemen-  
 1120 tations. *International Journal for Numerical Methods in Engineering*, *83*(10),  
 1121 1273–1311. Retrieved from <http://doi.wiley.com/10.1002/nme.2861> doi:  
 1122 10.1002/nme.2861
- 1123 Nishioka, T., & Atluri, S. (1982, 1). Numerical analysis of dynamic crack propaga-  
 1124 tion: Generation and prediction studies. *Engineering Fracture Mechanics*, *16*(3),  
 1125 303–332. Retrieved from [https://linkinghub.elsevier.com/retrieve/pii/](https://linkinghub.elsevier.com/retrieve/pii/0013794482901114)  
 1126 [0013794482901114](https://linkinghub.elsevier.com/retrieve/pii/0013794482901114) doi: 10.1016/0013-7944(82)90111-4
- 1127 Noda, H., & Lapusta, N. (2013). Stable creeping fault segments can become destructive as  
 1128 a result of dynamic weakening. *Nature*, *493*(7433), 518–521. Retrieved from [http://](http://dx.doi.org/10.1038/nature11703)  
 1129 [dx.doi.org/10.1038/nature11703](http://dx.doi.org/10.1038/nature11703) doi: 10.1038/nature11703
- 1130 Okubo, P. G. (1989). Dynamic rupture modeling with laboratory-derived constitutive re-  
 1131 lations. *Journal of Geophysical Research*, *94*(B9), 12321. Retrieved from [http://doi](http://doi.wiley.com/10.1029/JB094iB09p12321)  
 1132 [.wiley.com/10.1029/JB094iB09p12321](http://doi.wiley.com/10.1029/JB094iB09p12321) doi: 10.1029/JB094iB09p12321
- 1133 Pelties, C., de la Puente, J., Ampuero, J.-P., Brietzke, G. B., & Käser, M. (2012, 2).  
 1134 Three-dimensional dynamic rupture simulation with a high-order discontinuous  
 1135 Galerkin method on unstructured tetrahedral meshes. *Journal of Geophysical Re-*  
 1136 *search: Solid Earth*, *117*(B2), n/a-n/a. Retrieved from [http://doi.wiley.com/](http://doi.wiley.com/10.1029/2011JB008857)  
 1137 [10.1029/2011JB008857](http://doi.wiley.com/10.1029/2011JB008857) doi: 10.1029/2011JB008857
- 1138 Rice, J. R. (1993). Spatio-temporal complexity of slip on a fault. *Journal of Geophysical*  
 1139 *Research*, *98*(B6), 9885–9907. doi: 10.1029/93JB00191
- 1140 Rice, J. R. (2006, 5). Heating and weakening of faults during earthquake slip. *Journal*  
 1141 *of Geophysical Research: Solid Earth*, *111*(B5), n/a-n/a. Retrieved from [http://doi](http://doi.wiley.com/10.1029/2005JB004006)  
 1142 [.wiley.com/10.1029/2005JB004006](http://doi.wiley.com/10.1029/2005JB004006) doi: 10.1029/2005JB004006
- 1143 Rice, J. R., & Ben-Zion, Y. (1996, 4). Slip complexity in earthquake fault models. *Proceed-*  
 1144 *ings of the National Academy of Sciences*, *93*(9), 3811–3818. Retrieved from [http://](http://www.pnas.org/cgi/doi/10.1073/pnas.93.9.3811)  
 1145 [www.pnas.org/cgi/doi/10.1073/pnas.93.9.3811](http://www.pnas.org/cgi/doi/10.1073/pnas.93.9.3811) doi: 10.1073/pnas.93.9.3811
- 1146 Rice, J. R., & Ruina, A. L. (1983). Stability of Steady Frictional Slipping. *Journal*  
 1147 *of Applied Mechanics*, *50*(2), 343. Retrieved from [http://appliedmechanics](http://appliedmechanics.asmedigitalcollection.asme.org/article.aspx?articleid=1406945)  
 1148 [.asmedigitalcollection.asme.org/article.aspx?articleid=1406945](http://appliedmechanics.asmedigitalcollection.asme.org/article.aspx?articleid=1406945) doi:  
 1149 10.1115/1.3167042
- 1150 Rousseau, C. E., & Rosakis, A. J. (2009). Dynamic path selection along branched faults:  
 1151 Experiments involving sub-Rayleigh and supershear ruptures. *Journal of Geophysical*  
 1152 *Research: Solid Earth*, *114*(8), 1–15. doi: 10.1029/2008JB006173
- 1153 Ruina, A. (1983). Slip instability and state variable friction laws. *Journal of Geophysical*  
 1154 *Research*, *88*(B12), 10359–10370. doi: 10.1029/JB088iB12p10359
- 1155 Shibazaki, B., & Matsu'ura, M. (1992, 6). Spontaneous processes for nucleation, dynamic  
 1156 propagation, and stop of earthquake rupture. *Geophysical Research Letters*, *19*(12),  
 1157 1189–1192. Retrieved from <http://doi.wiley.com/10.1029/92GL01072> doi: 10.  
 1158 1029/92GL01072
- 1159 Taborda, R., & Bielak, J. (2011). Large-Scale Earthquake simulation: Computational  
 1160 seismology and complex engineering systems. *Computing in Science and Engineering*,  
 1161 *13*(4), 14–26. doi: 10.1109/MCSE.2011.19
- 1162 Thomas, M. Y., Lapusta, N., Noda, H., & Avouac, J.-P. (2014, 3). Quasi-dynamic versus  
 1163 fully dynamic simulations of earthquakes and aseismic slip with and without en-  
 1164 hanced coseismic weakening. *Journal of Geophysical Research: Solid Earth*, *119*(3),  
 1165 1986–2004. Retrieved from <http://doi.wiley.com/10.1002/2013JB010615> doi:  
 1166 10.1002/2013JB010615
- 1167 Tong, X., & Lavier, L. L. (2018, 12). Simulation of slip transients and earthquakes in finite  
 1168 thickness shear zones with a plastic formulation. *Nature Communications*, *9*(1). doi:  
 1169 10.1038/s41467-018-06390-z
- 1170 Tse, S. T., & Rice, J. R. (1986). Crustal earthquake instability in relation to the depth  
 1171 variation of frictional slip properties. *Journal of Geophysical Research*, *91*(B9), 9452.  
 1172 Retrieved from <http://doi.wiley.com/10.1029/JB091iB09p09452> doi: 10.1029/  
 1173 JB091iB09p09452
- 1174 Van Dinther, Y., Gerya, T. V., Dalguer, L. A., Mai, P. M., Morra, G., & Giardini, D.  
 1175 (2013). The seismic cycle at subduction thrusts: Insights from seismo-thermo-me-

- 1176           chanical models. *Journal of Geophysical Research: Solid Earth*, 118(12), 6183–6202.  
1177           doi: 10.1002/2013JB010380
- 1178   Y.-G. Li, & Leary, P. C. (1990). Fault zone trapped seismic waves. *Bulletin of the Seismo-*  
1179           *logical Society of America*, 80(5), 1245–127.
- 1180   Yang, H., & Zhu, L. (2010, 10). Shallow low-velocity zone of the San Jacinto fault from  
1181           local earthquake waveform modelling. *Geophysical Journal International*, 183(1),  
1182           421–432. Retrieved from [https://academic.oup.com/gji/article-lookup/doi/](https://academic.oup.com/gji/article-lookup/doi/10.1111/j.1365-246X.2010.04744.x)  
1183           10.1111/j.1365-246X.2010.04744.x doi: 10.1111/j.1365-246X.2010.04744.x
- 1184   Yang, H., Zhu, L., & Cochran, E. S. (2011, 8). Seismic structures of the Calico fault zone  
1185           inferred from local earthquake travel time modelling. *Geophysical Journal Interna-*  
1186           *tional*, 186(2), 760–770. Retrieved from [https://academic.oup.com/gji/article](https://academic.oup.com/gji/article-lookup/doi/10.1111/j.1365-246X.2011.05055.x)  
1187           -lookup/doi/10.1111/j.1365-246X.2011.05055.x doi: 10.1111/j.1365-246X.2011  
1188           .05055.x

**Tables**

| Parameter                                    | Symbol     | Value     |
|--|------------|-----------|
| Density (kg/m <sup>3</sup> )                 | $\rho$     | 2670.0    |
| Shear wave speed (km/s)                      | $c_s$      | 3.464     |
| Effective normal stress on fault (MPa)       | $\sigma_n$ | 50.0      |
| Critical slip distance (m)                   | $L$        | 0.008     |
| Plate rate (m/s)                             | $V_p$      | $10^{-9}$ |
| Reference slip rate (m/s)                    | $V_o$      | $10^{-6}$ |
| Initial slip rate (m/s)                      | $V_{init}$ | $10^{-9}$ |
| Reference friction coefficient               | $f_o$      | 0.6       |
| Depth extent of uniform VW region (km)       | $H$        | 15.0      |
| Width of transition (km)                     | $h$        | 3.0       |
| Rate and State parameter                     | $b$        | 0.015     |
| Rate and State parameter                     | $a_{max}$  | 0.025     |
| Rate and State parameter                     | $a_{min}$  | 0.010     |
| Fault length (km)                            | $W_f$      | 40        |
| Distance between two virtual boundaries (km) | $W_s$      | 1         |
| Loading distance (km)                        | $W_l$      | 40        |
| Depth (km)                                   | $L_z$      | 80        |

Table 1: Problem parameters for the SCEC SEAS Benchmark BP1-2D

## Figures

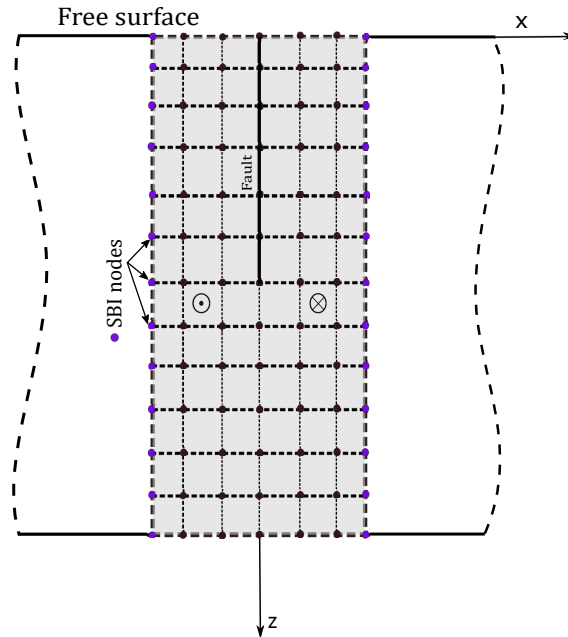


Figure 1: Illustration of the hybrid method with coupling of the FEM and SBI. A schematic illustration of the problem of our 2-D model, showing rate and state fault embedded in a heterogeneous sub-space subjected to anti-plane shear deformations. The balance equations within the region of interest are discretized with finite element model. The tractions on SBI nodes (blue) are computed using SBI scheme with known Green's function and applied on FEM (black) as traction boundary conditions on each side. The free surface presents a traction-free boundary condition.

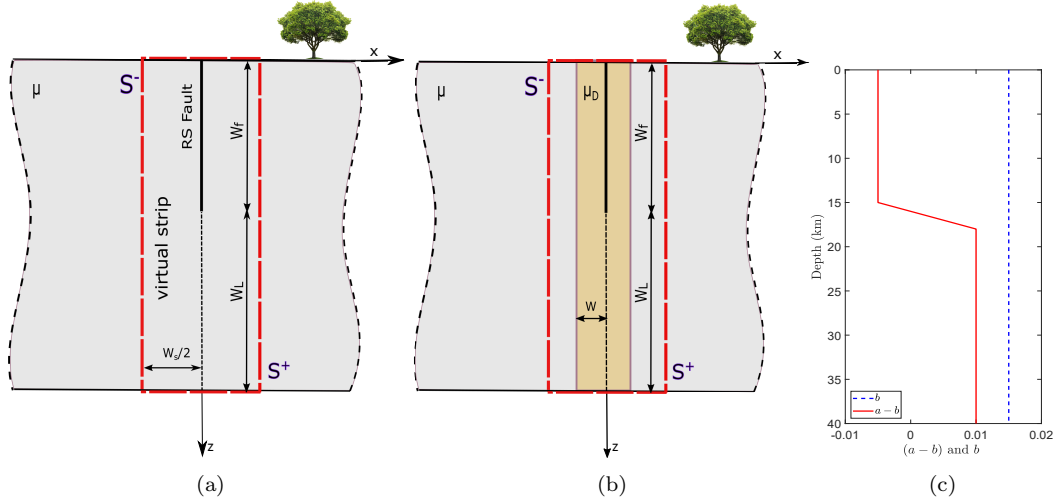


Figure 2: Problem setup. (a) The hybrid scheme setup for BP1-2D. The width of the finite element domain is  $W_s$ . The fault length is  $W_f$ . The loading is done beneath the fault at a rate  $V_p$  applied on length  $W_L$ , the depth  $L_z = W_f + W_l$ . A planar fault is embedded in a homogeneous, linear-elastic half-space with a free surface. The fault creeps at an imposed plate rate of  $V_p$  down to infinite depth. (b) Low-velocity fault zone hybrid scheme setup, where the damaged region is confined within width  $W$  and has a shear modulus  $\mu_D$ . The red box indicates the domain to be discretized using the FEM coupled with the SBI at the lateral boundaries. (c) The variability in the distribution of rate and state parameters  $(a - b)$  and  $b$  for both problems.

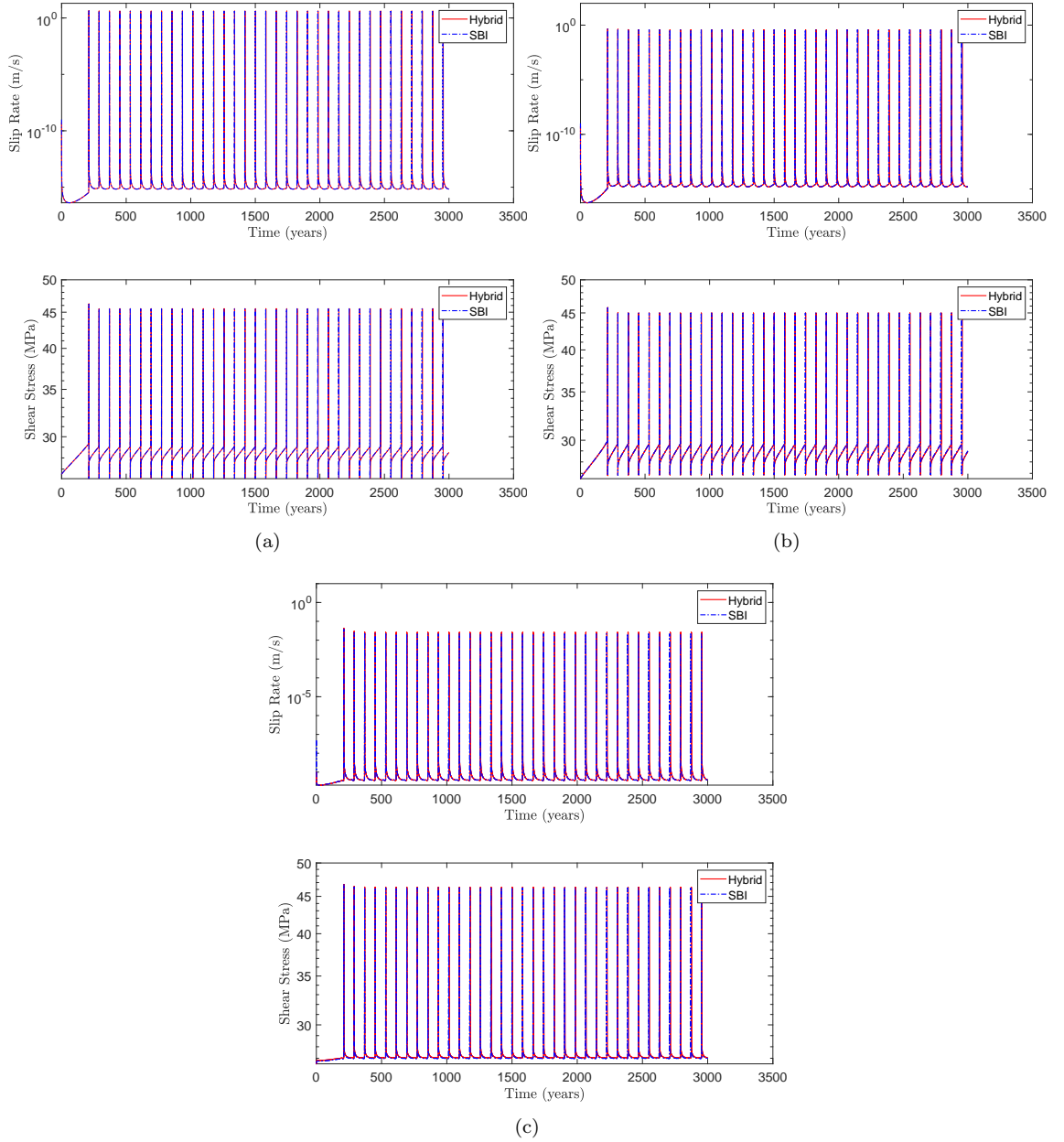


Figure 3: Results for SCEC SEAS Benchmark Problem BP-1 simulation comparing the hybrid method (in red) with the spectral boundary integral method (in blue). (a) Time history of the slip rate, and shear stress at the station on the free surface. (b) Time history of the slip rate, and shear stress at a station 7.5 km away from the free surface. (c) Time history of the slip rate, and shear stress at a station 17.5 km away from the free surface. All results show excellent agreement between the two methods.

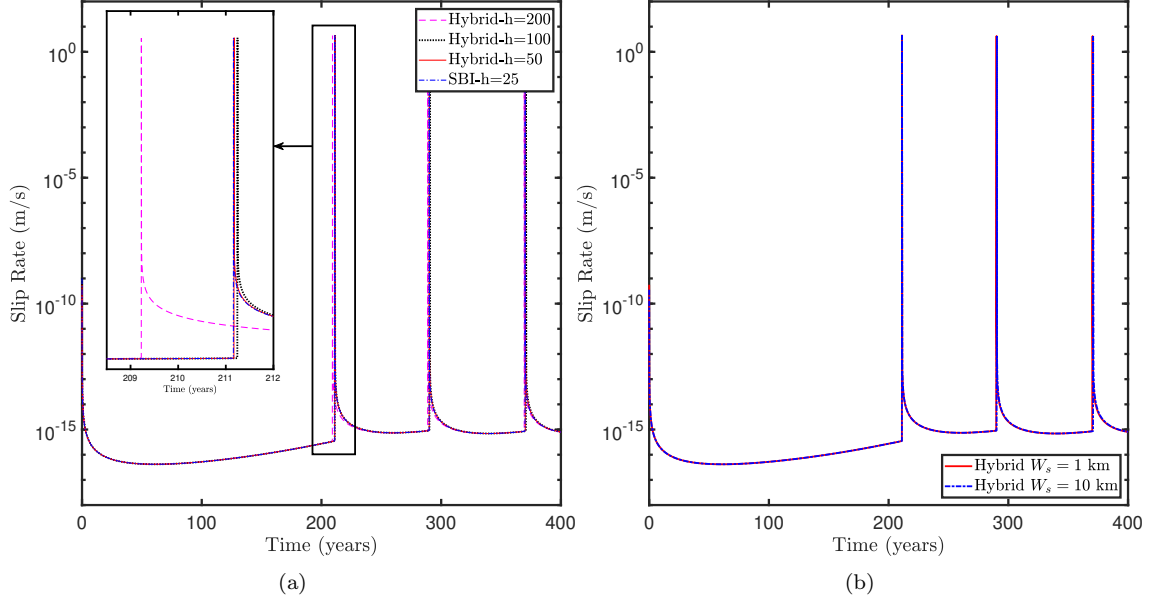


Figure 4: Convergence study for the hybrid scheme. (a) Surface slip rate on the fault as a function of time comparing the solution of the hybrid scheme against the pure SBI solution for various mesh sizes of FEM ( $h = 50$  m,  $100$  m, and  $200$  m). The results from the hybrid scheme matches the SBI solution for both seismic and inter-seismic periods, and converge to the SBI solution with refinement. (b) A 400-year time history of the surface slip rate on the fault comparing two different FEM strip  $W_s$  thicknesses,  $1$  km and  $10$  km. The results from the two different widths show that the solution does not vary with increased thickness and is insensitive to the location of the virtual boundaries.

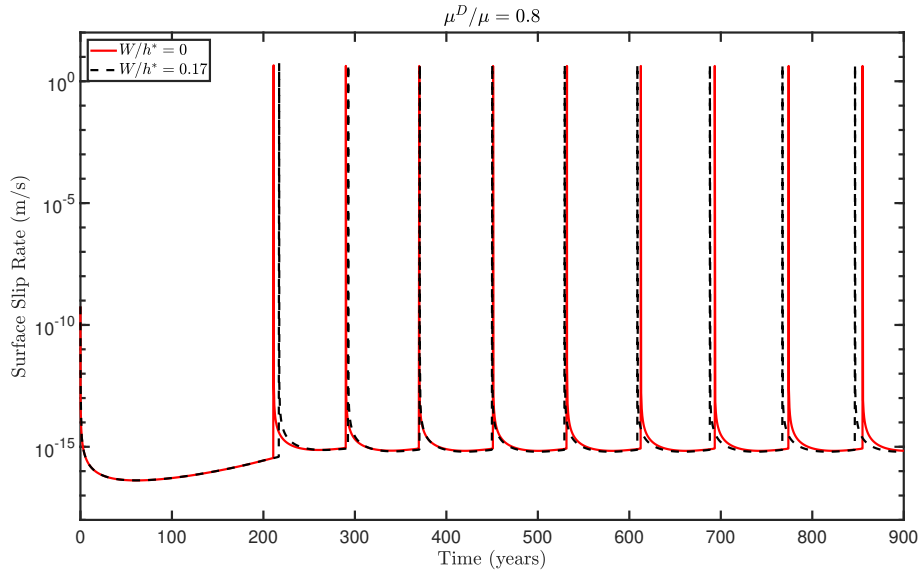


Figure 5: Surface slip rate history, illustrating the influence of a mild rigidity contrast on the earthquake sequence of the simulated problem. Shown are the results for the homogeneous case compared to the LVFZ with  $W/h^* = 0.17$  and  $\mu_D/\mu = 0.8$  under background plate loading  $V_p = 10^{-9}$  m/s. The two cases show approximately the same trend.

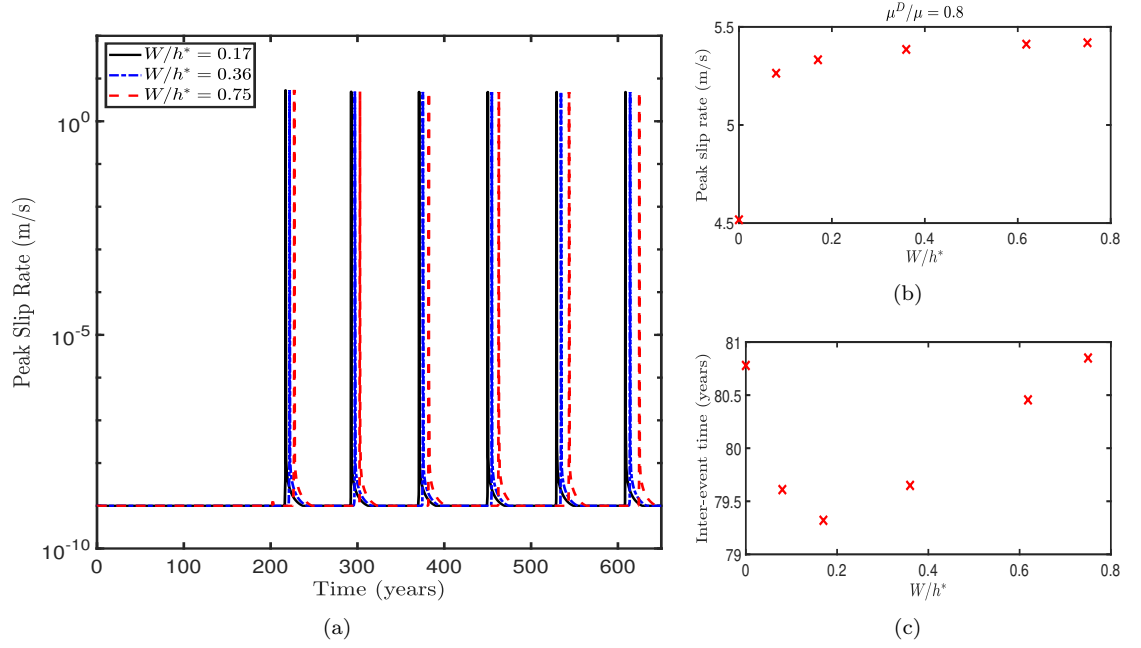


Figure 6: Effects of a low-velocity fault zone of width  $W$  on earthquake sequence. (a) Time history of peak slip rate demonstrating the shift in occurrence time for various LVFZ  $W/h^*$  at a mild rigidity contrast of  $\mu_D/\mu = 0.8$ . (b) The maximum peak slip rate during earthquake cycle as a function of  $W/h^*$ . A more pronounced increase in the peak slip rate is observed as the width of the LVFZ increases from zero to the order of the process zone, which is associated with a rapid decay in the effective shear modulus. Afterwards we observe a slow increase in the peak slip rate as the effective shear modulus, in the high frequency limit, approaches a constant value. (c) Inter-event time between successive earthquakes as a function of  $W/h^*$  computed after the cycle converges to a steady state, showing a non-monotonic dependency of inter-event time on LVFZ width.

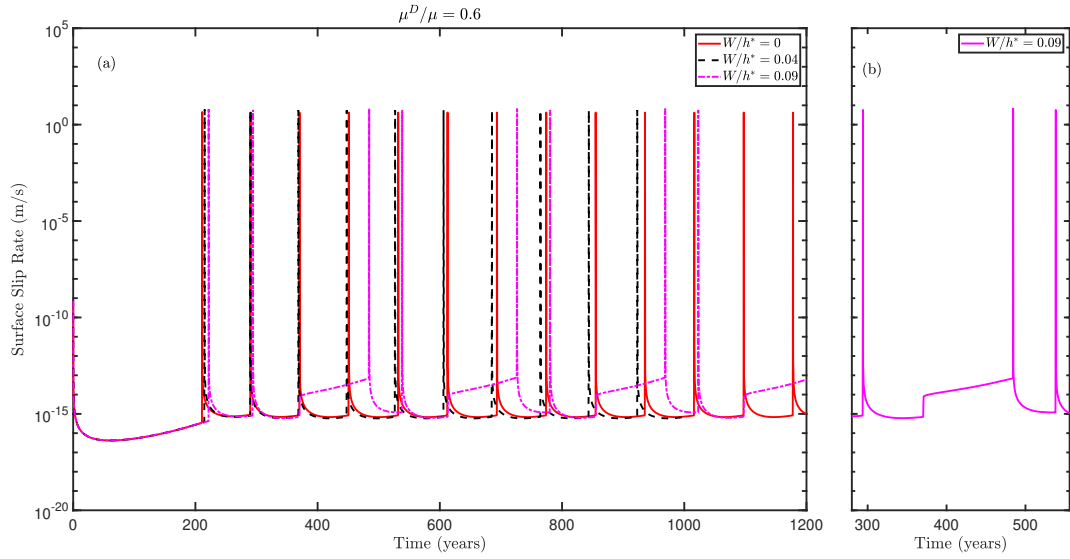
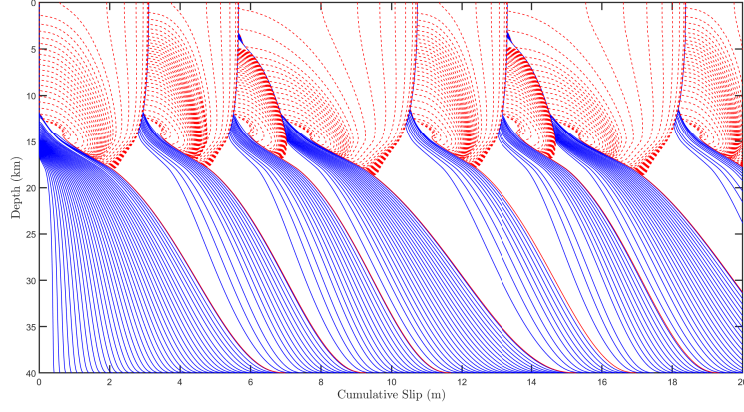
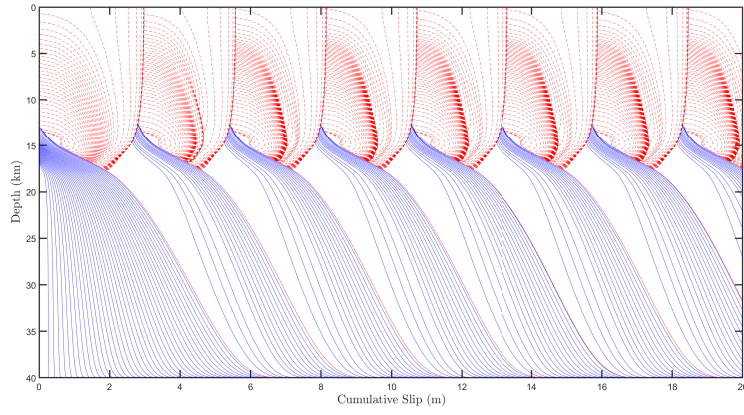


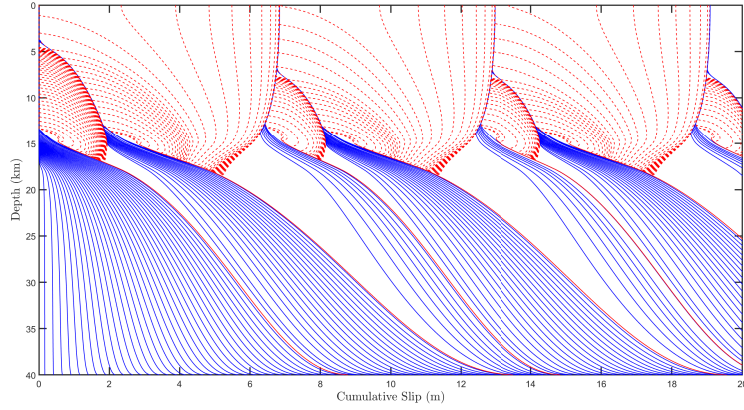
Figure 7: Surface slip rate time history for intermediate rigidity contrast  $\mu_D/\mu = 0.6$  with background plate loading  $V_p = 10^{-9}$  m/s. (a) Three different cases of varying  $W/h^*$ , showing an the impact of the low-velocity fault zone width on the earthquake cycle sequence. (b) A zoomed-in excerpt for the surface slip rate time history for  $W/h^* = 0.09$  between 280-550 years showing a kink in the surface slip rate during the sub-surface events, corresponding to an increase in the slip rate but was not high enough to reach seismic rates.



(a)



(b)



(c)

Figure 8: Snapshots of cumulative slip profiles for  $\mu_D/\mu = 0.6$ . Solid blue lines plotted at five-year intervals during aseismic slip when peak slip rate is lower than  $10^{-3}$  m/s; red lines plotted at every one second during quasi-dynamic rupture. (a) LVFZ with width  $W/h^* = 0.09$ . (b) LVFZ with width  $W/h^* = 0.65$ . (c) LVFZ with width  $W/h^* = \infty$ .

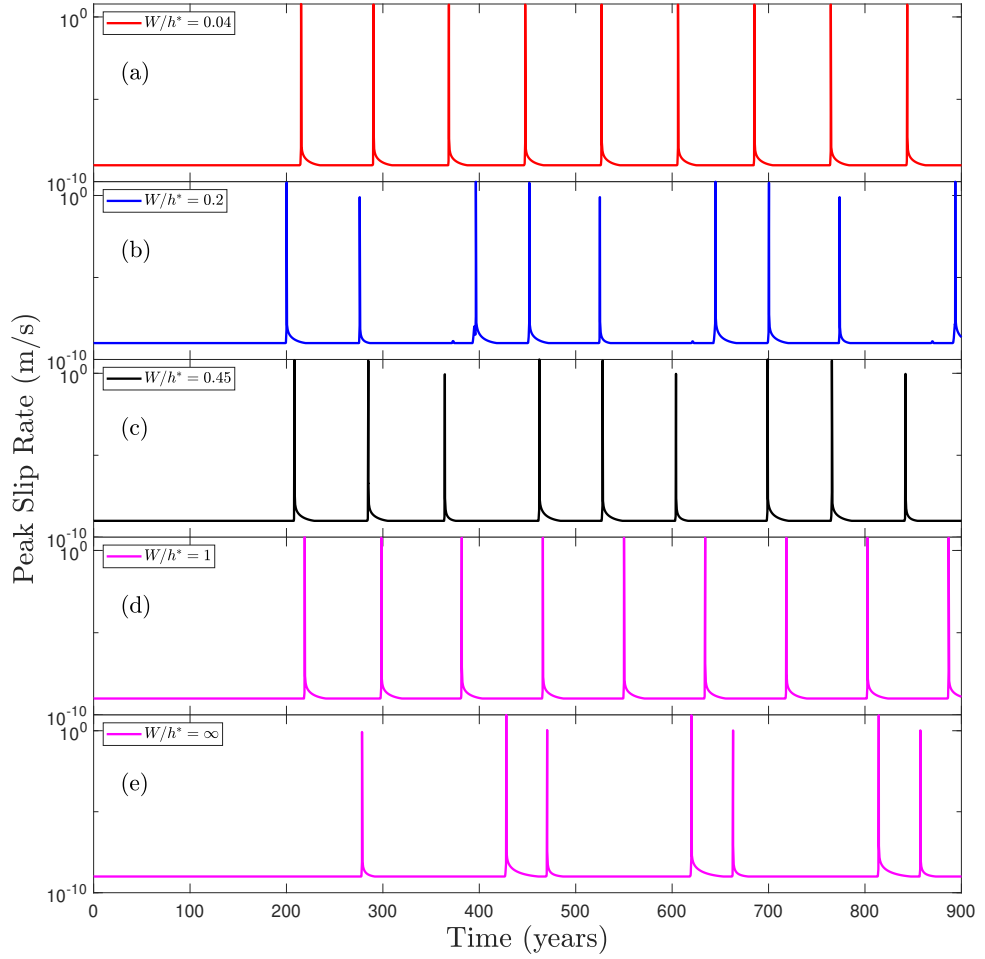


Figure 9: A comparison of the peak slip rate history for various low-velocity fault zone width  $W$  and  $\mu_D/\mu = 0.6$ , illustrating its impact on the earthquake sequence. (a) An earthquake cycle for  $W/h^* = 0.04$  showing a periodic sequence of events. (b-c) A complex earthquake sequence emerges that converges to three successive events followed by a delay. (d) An earthquake cycle for  $W/h^* = 1$  showing again a periodic sequence of events. (e) A sequence of alternating surface reaching and sub-surface events in a homogeneous bulk structure with  $\mu = 19.2$  GPa corresponding to a fully damaged media.

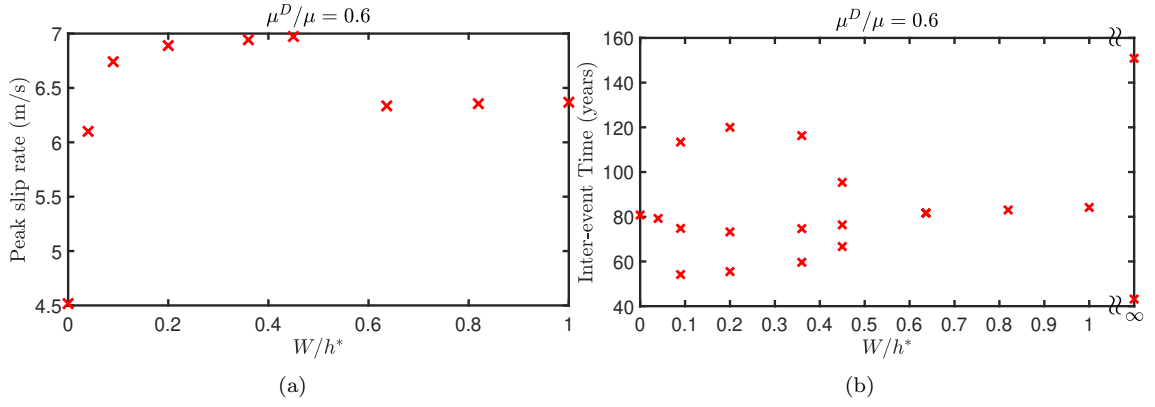


Figure 10: A comparison of the effect of  $W/h^*$  on a low-velocity fault zone with  $\mu_D/\mu = 0.6$  with emerging complexities. (a) The maximum peak slip rate as a function of  $W/h^*$ . The slip rate amplification is larger in this case compared to  $\mu_D/\mu = 0.8$ . It is also larger as LVFZ width increase, at least for sequences with both sub-surface and surface reaching events. (b) The inter-event time at a steady state capturing the periodicity of occurrences. Multiple points indicate cluster rather than single-event periodicity, whereas each cluster may consist of two or three seismic events.

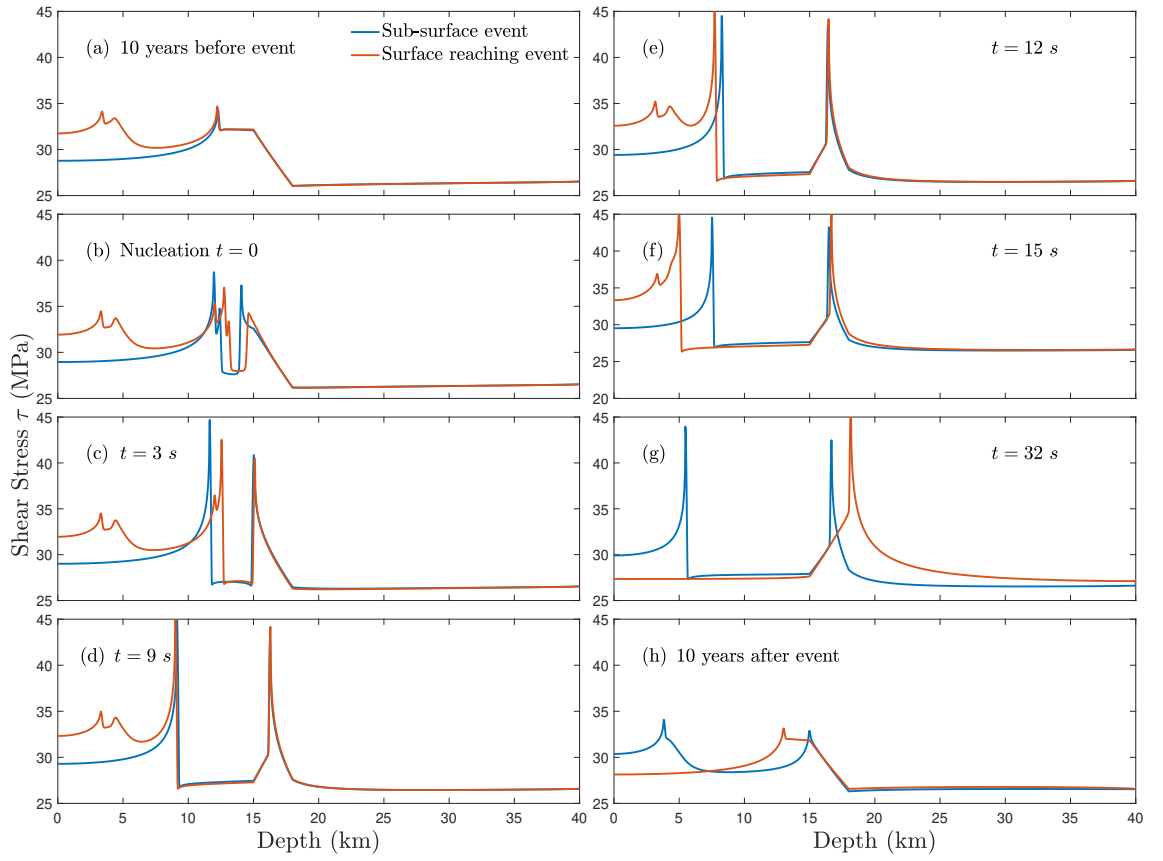


Figure 11: Snapshots of shear stress comparing a surface reaching event (red) and a sub-surface event (blue). (a) 10 years before the event. (b-g) During the event. (h) After the event. The sub-surface events contribute to a residual stress concentration in the vicinity of the rupture arrest. Demonstrated for  $W/h^* = 0.09$  and  $\mu_D/\mu = 0.6$ .

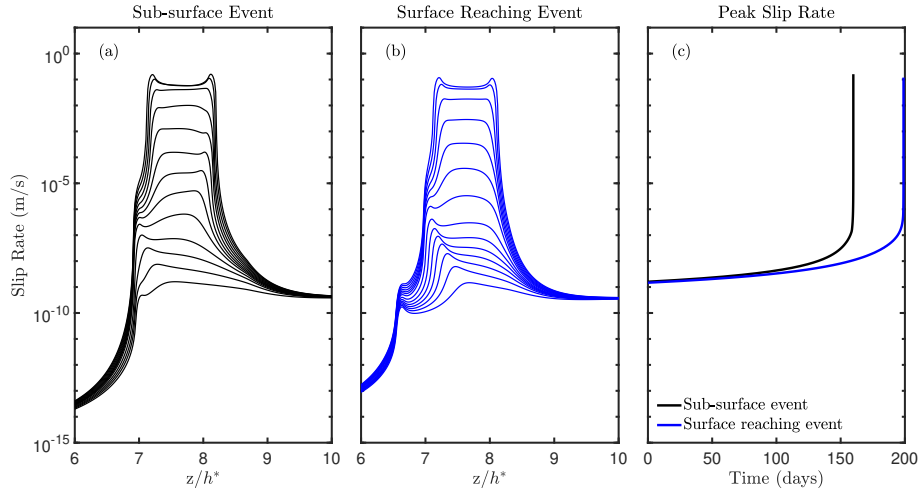


Figure 12: Comparison between the nucleation process in a sub-surface event and a surface reaching event. (a) Snapshots for slip rate as a function of depth ratio  $z/h^*$  for a sub-surface event. (b) Snapshots for slip rate for a surface reaching event, suggesting the nucleation process for both sub-surface and surface reaching events are similar. (c) The evolution of the peak slip rate as a function of time for each of the events, suggesting a similar trend for both events. The parameters are identical to those in Figure 11.

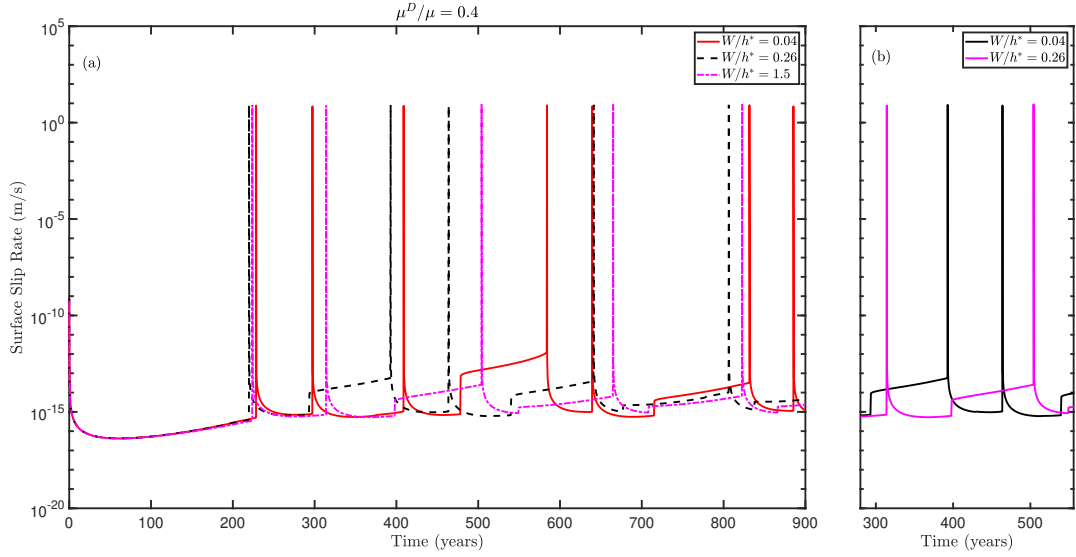


Figure 13: Surface slip rate time history shown for three different cases of varying  $W/h^*$  at strong rigidity contrast of  $\mu_D/\mu = 0.4$  with background plate loading  $V_p = 10^{-9}$  m/s. (a) The low-velocity fault zone width alters the characteristics of the seismic cycle. (b) A zoomed-in excerpt for the surface slip rate time history for  $W/h^* = 0.04 - 0.26$  between 280-550 years showing the slight increase in surface slip rate during sub-surface events.

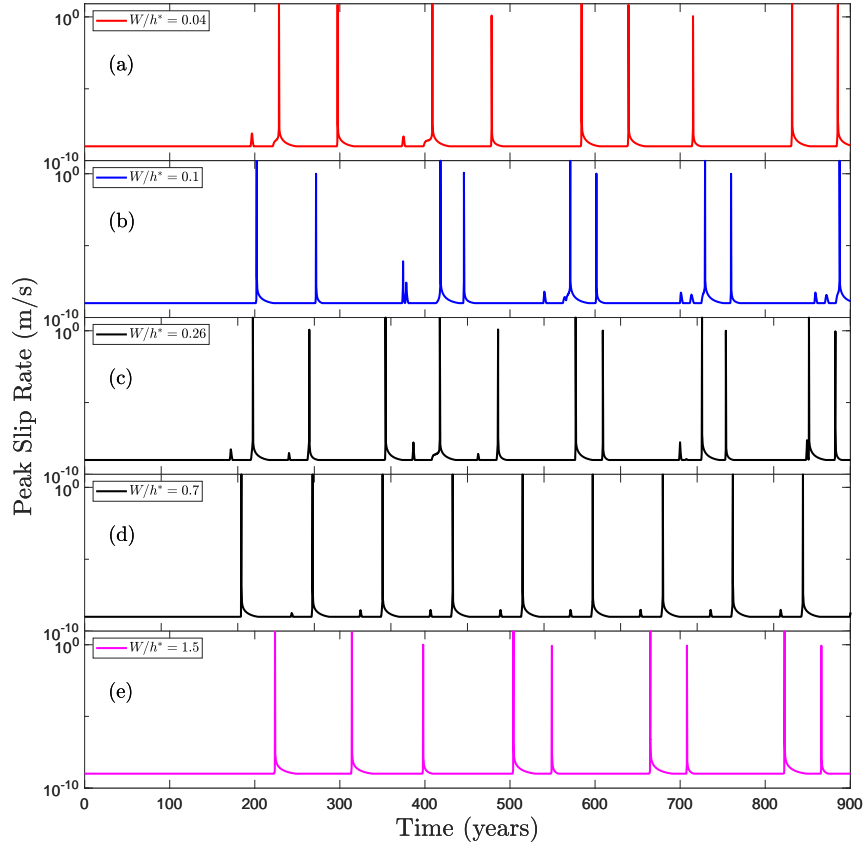


Figure 14: A comparison of the peak slip rate history for various low-velocity fault zone width  $W$  and  $\mu_D/\mu = 0.4$ , illustrating its impact on the earthquake sequence. (a) A complex earthquake sequence emerges that converges to three successive events followed by a delay for  $W/h^* = 0.04$ , similar to Figure 9c. (b-c) An alternative earthquake sequence emerges that converges to two successive events followed by a delay for  $W/h^* = 0.1 - 0.26$ . (d) An earthquake cycle for  $W/h^* = 0.7$  consisting of a sequence of periodic events. (e) A steady-state behavior of two successive events followed by a delay for  $W/h^* = 1.5$ .

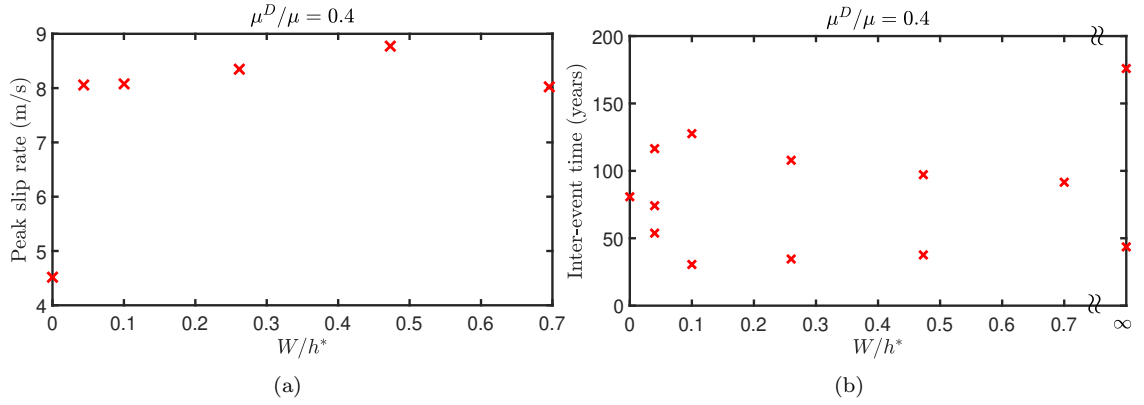


Figure 15: A comparison for the effect of  $W/h^*$  on a low-velocity fault zone with  $\mu_D/\mu = 0.4$  with emerging complexities. (a) The maximum peak slip rate as a function of  $W/h^*$  showing slip rate amplification relative to the homogeneous case. (b) The inter-event time at a steady state capturing the periodicity of occurrences. Multiple points indicate cluster rather than single-event periodicity, whereas each cluster may consist of two or three seismic events.

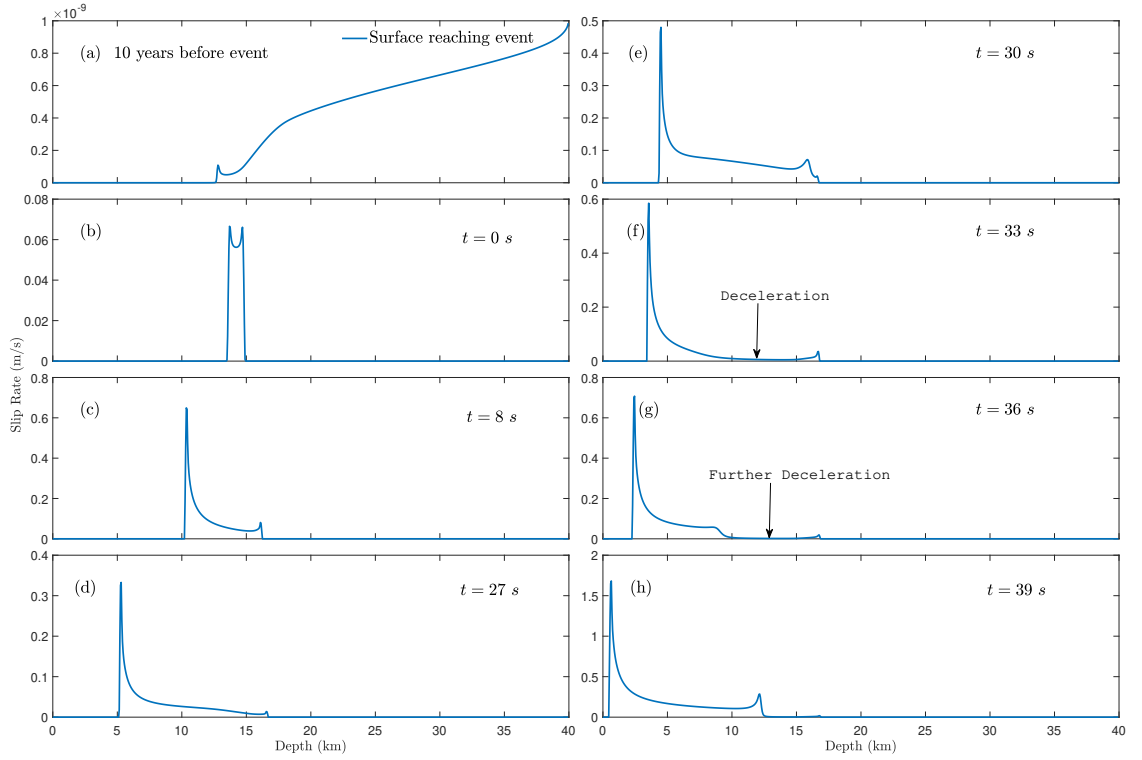


Figure A1: Snapshots of slip rate for  $\mu_D/\mu = 0.6$  and  $W/h^* = 0.65$ . (a) 10 years prior to the event occurrence. (b-e) Quasi-dynamic rupture propagation. (f) At  $t = 33$  s the rupture decelerates near the VS region. (g) Further deceleration near the VS region. (h) One rupture front propagates to the free surface while another front re-emerges and propagates backward toward the VS region.

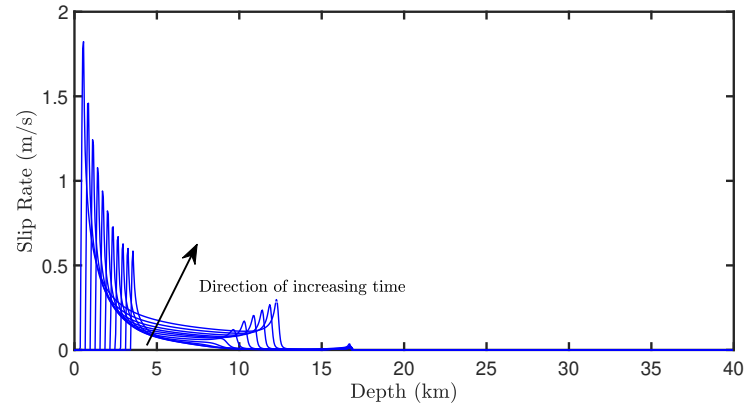


Figure A2: Snapshots of slip rate for  $\mu_D/\mu = 0.6$  and  $W/h^* = 0.65$  between  $t = 33 - 39$  s, showing the rapid back propagating front.